The Journal of the Astronautical Sciences (2022) 69:651–691
https://doi.org/10.1007/s40295-022-00325-z

ORIGINAL ARTICLE

Visibility Study in a Chief-Deputy Formation for CMB Polarization Missions

Juan Bermejo-Ballesteros[1] · Javier Cubas[1] · Francisco Casas[2] · Enrique Martínez-González[2]

Accepted: 5 April 2022 / Published online: 29 April 2022

Abstract

Scientific instruments on board satellites are becoming increasingly sensitive, making it imperative to submit these instruments to a thorough calibration. In-flight calibration could be largely improved by using an ancillary microsatellite flying in formation with the main satellite and emitting a well-defined and known reference signal. Due to the main satellite attitude motion, the calibration satellite and therefore, its calibration signal, will only enter the instrument FoV (Field of View) at certain instants. It is not intuitive how frequently and during how much time this will happen, or how this depends on the scan strategy. In the present work, the available time for calibration and its characteristics in terms of total, mean, and maximum duration are studied, deriving analytical expressions for these quantities. These expressions are validated numerically and allow us to assess the impact of different scan strategies and to evaluate the most suitable region to locate the calibration satellite. The focal plane of the instrument is also modelled to evaluate the calibration process at detector level, calculating the number of detectors viewed and the direction of the polarized signal that they received. For this last analysis, only numerical methods have been employed. The tools are finally used in a case study in order to show how they can be employed to test, evaluate, and optimize scanning strategies and relative positions. The tools presented in this work can be easily adapted to evaluate more generally the characteristics of the observation of each point in the sky for a given scan strategy and instrument FoV.

Keywords formation flight · Visibility · Access time · Calibration · Microwaves calibration · Scan strategy

✉ Juan Bermejo-Ballesteros
juan.bermejo@upm.es

[1] Instituto Universitario "Ignacio Da Riva" (IDR/UPM), Universidad Politécnica de Madrid, Plaza Cardenal Cisneros 3, Madrid E-28040, Spain

[2] Instituto de Física de Cantabria (CSIC-UC), Avda. de los Castros s/n, Santander E-39005, Spain

Nomenclature

T_{total}	Total access time.
T_{mean}	Mean access time.
T_{max}	Maximum access time.
T_{sim}	Simulated time.
T_{comb}	Period of the combined motion of precession and spin motions.
T_{prec}	Precession motion period.
T_{spin}	Spin motion period.
T_{access}	Access time.
ϕ	Spin angle.
ψ	Precession angle.
Ω	Precession speed.
ω	Spin speed.
α	Precession axis angle.
β	Instrument axis angle.
δ	Half-angle of instrument FoV.
ζ	Spatial separation between sequential trace rings.
FoV	Field of View.
LoS	Line-of-sight.
ρ	Percentage of viewed detectors.
$G(\xi)$	Angular coverage parameter.
$C_{0,b}$	Satellite attitude matrix.
$C_{b,inst}$	Instrument mounting matrix.
$C_{0,inst}$	Instrument attitude matrix.
$\mathbf{q}(t)$	Instrument pointing direction.
$\mathbf{r}_{cd}$	Deputy position relative to the chief.
$\mathbf{p}_{cd}$	Unit vector of the deputy position relative to the chief.
$\mathbf{r}_{deputy}$	Deputy position vector.
$\mathbf{r}_{chief}$	Chief position vector.
φ, θ	Coordinates in the pseudo-inertial reference frame.
φ^*, θ^*	Coordinates in the instrument frame.
φ_v	Angle between instrument direction and X_0-axis.
θ_φ	Half-arc angle of directions with the same φ coordinate inside the FoV
θ^*_φ	Half-arc angle of a direction trajectory inside the FoV.
$\mathbf{p}_\varphi$	Arbitrary direction.
$\mathbf{q}^*$	Equivalent vertical motion of the instrument.
$\mathbf{q}_0$	Starting position of the instrument direction.
$\mathbf{q}$	Instrument pointing direction.
$\mathbf{u}_{spin}$	Spin axis direction.
R	Rotation matrix around the spin axis.
f_t	Average fraction of directions inside the FoV in one spin period.
f_m	Fraction of directions that have been inside the FoV after one spin period.
φ_e, θ_e	Coordinates of exterior curve.
φ_i, θ_i	Coordinates of interior curve.
N	Number of accesses.

$\mathbf{q}_e$	Exterior curve direction.
$\mathbf{q}_i$	Interior curve direction.
$\mathbf{n}$	Unitary normal to the trace.
x_e, y_e, z_e	Cartesian coordinates of exterior curve.
x_i, y_i, z_i	Cartesian coordinates of interior curve.
$\mathbf{q}'$	Derivate of instrument pointing direction.
t_{max}	Optimum access time.
$\varphi^*_{t_{max}}$	Value of φ^* coordinate to achieve t_{max}.
t_1, t_2, t_3	Maximum access time according to φ coordinate.
τ	Auxiliary angle to describe $\mathbf{v}_{prec}$.
γ	Projection of $\mathbf{v}_{prec}$ over $\mathbf{v}_{spin}$.
$\mathbf{v}_{prec}$	Precession velocity unitary vector.
$\mathbf{v}_{spin}$	Spin velocity unitary vector.
D	Distance between satellites.
d	Size of emitting source.
ε	Angular size.
λ	Wavelength of signal.
CMB	Cosmic Microwave Background.
Re[x]	Real part of x.
dT	Time step.

1 Introduction

The scientific instruments on board satellites are becoming increasingly sensitive. To obtain measurements with an accuracy in line with such sensitivity, it is necessary to apply exhaustive calibration processes and error reduction algorithms to mitigate the systematic errors.

The calibration process is normally carried out prior to the flight and also during the mission. Each case presents its own limitations. Pre-flight calibration is not always capable of reproducing the mission environment or the signal to be measured due to the laboratory constraints (size, technology, etc.). Furthermore, after calibration, the satellite experiences different environmental conditions during launch, orbital transfer and eclipses, with subsequent thermal loads and vibrations, which can result in slight calibration drifts. During the mission, the main obstacle is that the signals from natural sources (moons, planets, compact objects, or even galaxies) are not known with the required accuracy for ultra-sensitive polarization missions observing in the microwave range [6, 12, 16] and, due to their scanning strategies to cover the whole sky, they do not always allow for the calibration of the instrumentation as required. For example, precision of the order of arc-minutes in the polarization angle are needed in such experiments, while the main polarization calibrator, Messier-1 (Tau A), is known with an error of about 0.5 degrees. If more precise scientific goals are to be achieved with sufficient success, a more robust in-flight calibration must be addressed for future missions.

One well-known example of this issue is the case of Cosmic Microwave Background (CMB) space missions. These telescopes measure the microwave signals that arrive from all directions of space, and that contain very valuable information about the origins of the universe. The primordial CMB signal was produced when the universe was about 380,000 years old and has a black-boby spectrum that, at present, peaks in the microwave range at about 160 GHz. Its tiny anisotropies in temperature and even dimmer ones in polarisation contain a wealth of information about the origin, matter and energy content, and the evolution of the universe. However, their measurement represents a very difficult challenge and requires the use of ultra sensitive telescopes with very accurate calibration procedures and an exquisite control of systematic effects. Some telescopes use the signal arriving from Jupiter as a reference for CMB intensity calibration, but it cannot be used for polarization calibration as it is not polarized.

In-flight calibration could be largely improved by using an ancillary microsatellite which would fly in formation with the main satellite and would emit a precisely characterised reference signal. This concept was initially proposed to calibrate Ground-based CMB telescopes [13] and has been extended for CMB satellites located in Sun-Earth L_2 [5]. This location is commonly used for astronomical missions due to its thermally stable environment (ideal for cryogenic missions), low acceleration, and the possibility of observing the sky continuously without interference from the Earth, or the Moon [7, 12, 16]. These CMB telescopes have a given scan strategy, which defines its attitude motion in order to cover all the sky and collect data according to its scientific objectives [4, 9, 20].

The formation would be a chief/deputy formation, in which the chief (main satellite) moves independently while the deputy (ancillary satellite) locates itself around the chief, keeping the formation. During operations, the calibration satellite would stay out of sight, so it does not interfere with the scientific observations. Then, when calibration is required, the deputy would move to a predefined location so the calibration signal could reach the chief's instrument. The extent of the sky region that is seen by the instrument at a given moment is called Field of View (FoV). Therefore, assuming that the deputy emits its calibration signal pointing always to the main satellite, the calibration will only occur when the deputy is inside the instrument FoV. Due to the chief's scan strategy, this only occurs in certain instants, and it is not intuitive when and how frequently it will happen. Such an event will be called here an 'access' and it can be characterized by its frequency, duration, and how effective it can be for calibration. These features depend mainly on the relative position of the deputy and the scan strategy followed by the chief.

The main goal of this article is to study the available time for calibration and its characteristics in terms of maximum and mean duration. This study will enable us to know which regions of space are more suitable to place the calibration satellite relative to the main satellite during the calibration phase. These aspects have been partially studied previously [3] and here a more complete study is presented.

To carry out the analysis, the direction at which the instrument is pointing over time has been modelled (Sect. 2) as well as the detectors geometrical disposition in the focal plane and the trajectory of the calibration signal through it (Sect. 4). In order to quantify the performance of a certain relative position, a set of parameters have been defined

based on the access features. These parameters describe two main aspects of the accesses: their temporal characteristics and how effective they can be for calibration. The former aspect is assessed in Sect. 3 through an analytical and numerical analysis that reports the number, frequency, and duration of the accesses. For the later aspect, analysed in Sect. 4, the signal received by the main satellite instrument is evaluated regarding the percentage of detectors that receive the signal and whether they are calibrated at different polarization angles. The complexity added by the instrument model implies the use of numerical methods for this aspect. The methodology described has been applied in Sect. 5 to an example mission, assessing the evolution of the parameters according to the variation of the scan strategy parameters and identifying suitable regions where the deputy can be placed. Finally, the conclusions are summarized in Sect. 6. All the methods presented here have been implemented in Python. Both the code and the results are accessible in an open GitLab repository [2], where other related works can also be found.

2 Scanning Strategy and Relative Position

The first step has been the modelling of the main satellite attitude motion to determine the instrument attitude and its pointing over time. The model used to describe the main satellite attitude is based on a simplified version of the one presented in [20]. In this case, only four parameters are used: the spin motion period (T_{spin}), the precession motion period (T_{prec}), the precession axis angle (α), and the instrument axis angle (β). The satellite spins around its main axis (spin axis) with a time period of T_{spin}. Simultaneously, the spin axis, which is separated by angle α from the precession axis, rotates around it with a time period of T_{prec}. The instrument line-of-sight (LoS) is separated by angle β from the spin axis and has a circular FoV with a half-angle of δ. The attitude of the satellite is defined with respect to a pseudo-inertial frame of reference (0) centered in the main satellite. Although this frame would not be inertial due to the satellite orbital motion, it can be considered as such for shorts period of time. The frame is shown along an scheme of the attitude motion in Fig. 1. The X_0-axis of the pseudo-inertial frame, which coincides with the precession axis, is parallel to the Sun direction and it is positive towards deep space. The Y_0 and Z_0 axes complete the right-handed frame and their direction can be chosen arbitrarily.

The attitude of the satellite can be described with an Euler angle sequence (1-3-1) in which the three angles (ψ, α, ϕ) are directly related to the scan strategy parameters, with ϕ being the angle rotated due to spin (2) and ψ the angle rotated due to precession (3). The equations (2) and (3) also define the spin speed (ω) and the precession speed (Ω). Then, the attitude matrix, as a function of three of the scan strategy parameters (T_{spin}, T_{prec} and α), is [8]

$$C_{0,b} = \begin{bmatrix} c_\alpha & c_\phi s_\alpha & s_\phi s_\alpha \\ -c_\psi s_\alpha & c_\psi c_\alpha c_\phi - s_\psi s_\phi & c_\psi c_\alpha s_\phi + s_\psi c_\phi \\ s_\psi s_\alpha & -s_\psi c_\alpha c_\phi - c_\psi s_\phi & -s_\psi c_\alpha s_\phi + c_\psi c_\phi \end{bmatrix}, \tag{1}$$

where

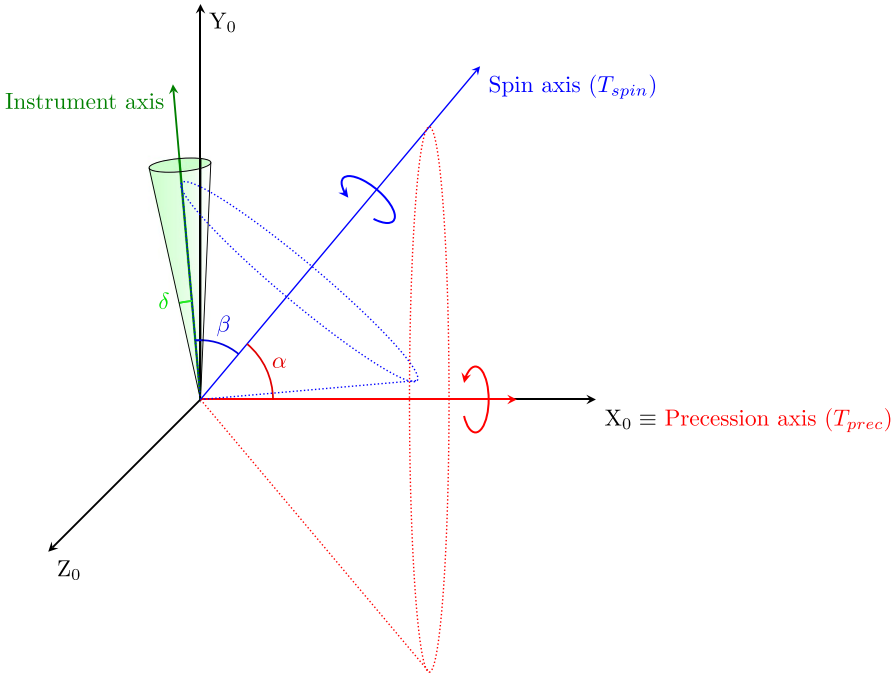

Fig. 1 Pseudo-inertial coordinate frame (0) and attitude motion scheme

$$\phi = \omega t = \frac{2\pi}{T_{spin}} t, \tag{2}$$

$$\psi = \Omega t = \frac{2\pi}{T_{prec}} t. \tag{3}$$

The attitude matrix (1) relates the orientation of the satellite body frame (b) and the pseudo-inertial reference frame (0). The instrument frame (*inst*) is defined as follows: its X_{inst}-axis is the instrument line of sight and the $Y_{inst}Z_{inst}$-plane corresponds to the plane where the detectors are located. The orientation of the instrument frame with regard to the satellite body frame is expressed by the mounting matrix

$$C_{b,inst} = \begin{bmatrix} c_\beta & s_\beta & 0 \\ -s_\beta & c_\beta & 0 \\ 0 & 0 & 1 \end{bmatrix}, \tag{4}$$

which consist of a rotation of angle β around satellite Z_b-axis. Thus, the attitude of the instrument is obtained by combining the satellite attitude matrix (1) and the mounting matrix (4) like

$$C_{0,inst} = C_{0,b} C_{b,inst}. \tag{5}$$

The instrument pointing direction can be obtained directly from the orientation of the instrument X_{inst}–axis as

$$\mathbf{q}(t) = C_{0i} \begin{Bmatrix} 1 \\ 0 \\ 0 \end{Bmatrix}. \tag{6}$$

As time passes, the line of sight of the instrument creates a pattern of observation over the celestial sphere. The morphology of this trace depends on the four parameters of the scan strategy. The orthographic projection of the instrument axis on the reference frame Y_0Z_0-plane is shown in Fig. 2 as an example of scan pattern. Note that the area swept by the FoV is not plotted. The scan strategy parameters choice is subjected to some constraints to ensure a complete and adequate observation of the sky [20]. For example, the sum of α and β defines the extent of the celestial sphere observed for a fixed direction of the precession axis. For a satellite orbiting L_2, where the precession axis usually points towards anti-Sun direction, it is necessary that $\alpha + \beta \geq 90°$ to observe the entire sky after six months. However, this sum should not be much higher to avoid pointing towards the Sun. Other constraints are the ratio between T_{spin} and T_{prec}, which defines the spatial separation between the sequential rings that are mapped in each spin turn and can be related to the FoV size, or the value of the sampling frequency, that must be high enough to sample the sky with the required accuracy and thus establishes a lower limit on T_{spin}. The scan strategy parameters used in the following examples are similar to to those used in previous and future CMB missions [6, 7, 11, 12, 17].

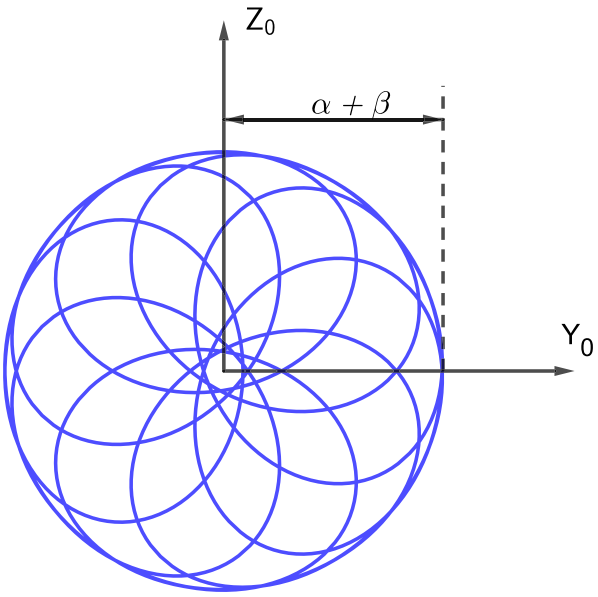

Fig. 2 Orthographic projection of the scan pattern for $\alpha = 45°$, $\beta = 50°$, $T_{spin} = 10$ min, and $T_{prec} = 90$ min

Once the sum constraint of α and β is set, the trace geometry will differ according to whether $\alpha < \beta$ or the contrary, as shown in Fig. 3. In the former case, the instrument line of sight encircles the precession axis in each spin rotation; while in the latter case it does not. In both cases, the minimum angle that the line of sight forms with the precession axis (the origin) is $|\alpha - \beta|$. Due to this, if the difference between both angles is high, the trace does not pass close to the precession axis, leaving a circular region without any crossover.

The relation between the periods of the spin and precession motions will also influence the geometry of the trace and is chosen carefully to avoid undesired effects and to ensure adequate coverage of the sky [18, 20]. As previously said, the ratio between the period of both motions defines the spatial separation ζ between the sequential rings of the trace

$$\frac{T_{spin}}{T_{prec}} = \frac{\zeta}{2\pi \sin \alpha}. \tag{7}$$

This separation can be chosen to be less than the FoV size (δ) to allow continuous mapping of the sky. Additionally, as both motions are periodic, their combined motion will also be periodic as long as the periods are related by a rational number (i.e., they are commensurable), in which case the pattern will repeat itself. In general, a higher period of the combined movement will produce a finer pattern, providing a more uniform coverage of the sky, since it will be necessary a larger amount of time until the trace starts repeating itself. Thus, the access duration of those points in the sky at the same angular distance from the precession axis will become more uniform. The combined period (T_{comb}) can be calculated as the least common multiple of both periods. This behaviour can be observed in Fig. 4, where a slight variation of the parameter T_{prec} changes the coverage considerably as the

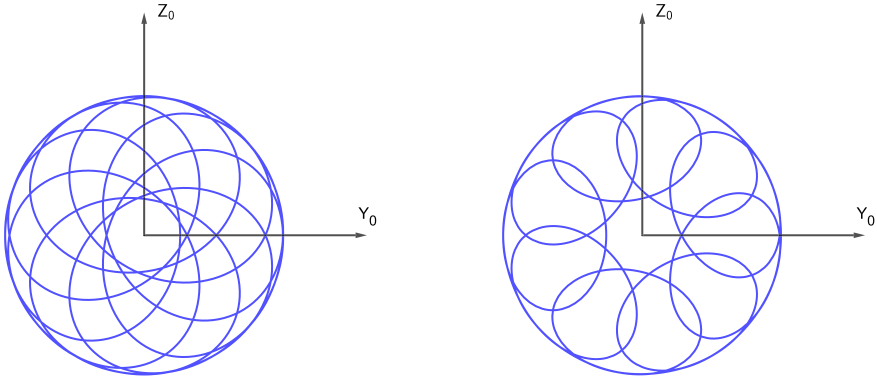

(a) $\alpha < \beta$ ($\alpha = 40°$ and $\beta = 55°$). (b) $\alpha > \beta$ ($\alpha = 55°$ and $\beta = 40°$).

Fig. 3 Change of the scan pattern morphology according to the relation between angles α and β. In both cases $T_{spin} = 10$ min and $T_{prec} = 90$ min

combined motion period rises. In Fig. 4(a), the combined period is $T_{comb} = 190$ min while in Fig. 4(b) the resulting period is $T_{comb} = 970$ min. In the first case, for points separated by 45° from the precession axis and $\delta = 7.5°$, the variations of the mean duration of the accesses is much higher, reaching a difference of 14 s, than in the second case, where the maximum differences is roughly 3 s.

As shown in Fig. 4, the pattern of the trace becomes increasingly uniform as the combined period of the two motions grows. Ideally, if such a period is infinite, this distribution will be fully axial-symmetric around the precession axis. Under this condition, the results of the visibility parameters can also be expected to have axial-symmetry around the precession axis. This simplification will be assumed in the analytical study.

Once the scan strategy is fixed, the access features will vary according to the relative positioning between deputy and chief. The deputy position relative to that of the chief is defined by the vector connecting both satellites

$$\mathbf{r}_{cd} = \mathbf{r}_{deputy} - \mathbf{r}_{chief}. \tag{8}$$

In this analysis, the distance separating the satellites is not relevant. For clarity the unit vector, defined as

$$\mathbf{p}_{cd} = \frac{\mathbf{r}_{cd}}{|\mathbf{r}_{cd}|} \tag{9}$$

is used instead. This unit vector represents the direction of the deputy on the sky as seen from the chief's perspective (5). This direction can be expressed in terms of two coordinates (φ, θ) as

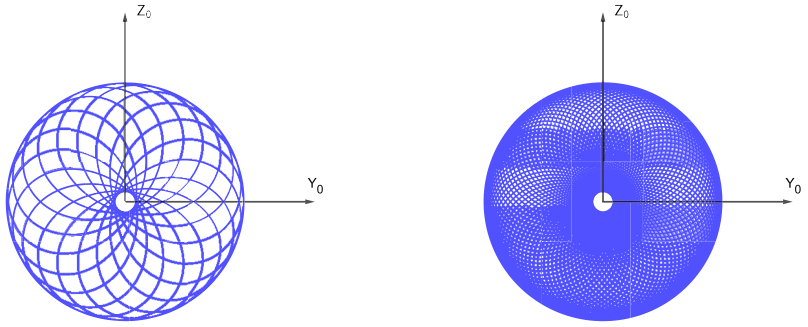

(a) $T_{spin} = 10$ min, $T_{prec} = 95$ min. (b) $T_{spin} = 10$ min, $T_{prec} = 97$ min.

Fig. 4 Change in the scan pattern due to the value of the combined motion period. For (**a**), the resulting period of the combined motions is $T_{comb} = 190$ min while for (**b**), the resulting period is $T_{comb} = 970$ min. In both cases $\alpha = 45°$ and $\beta = 50°$

$$\mathbf{p}_{cd} = \begin{Bmatrix} \cos\varphi \\ \sin\varphi\sin\theta \\ \sin\varphi\cos\theta \end{Bmatrix}, \tag{10}$$

with φ being the angular separation with X_0-axis, which here coincides with the precession axis, and θ the angle between the Z_0-axis and the projection of $\mathbf{p}_{cd}$ on Y_0Z_0 -plane. The use of these coordinates will help to derive the analytical expressions and facilitate the interpretation of the results. Axial-symmetry is equivalent to being independent of the θ coordinate; and the φ coordinate represents the angular separation from the precession axis. The defined vectors and the coordinates definition are shown in Fig. 5.

2.1 Numerical Modelling

For the numerical analysis, the space of possible directions has been discretized and used to detect when accesses will occur in each position. The results obtained are processed to calculate the parameters of interest. Every orientation vector obtained from the discretization represents a different relative position of the deputy regarding the chief i.e., a point in the sky. Furthermore, this orientation vector defines the line of sight between both satellites, which is used to detect when an access is happening.

For the analysis of a time period, the attitude of the satellite and the instrument is generated with a fixed sample time and stored for subsequent analysis. The time step used in such discretization ($dT = 0.1$ s in this work) establishes the precision of the results.

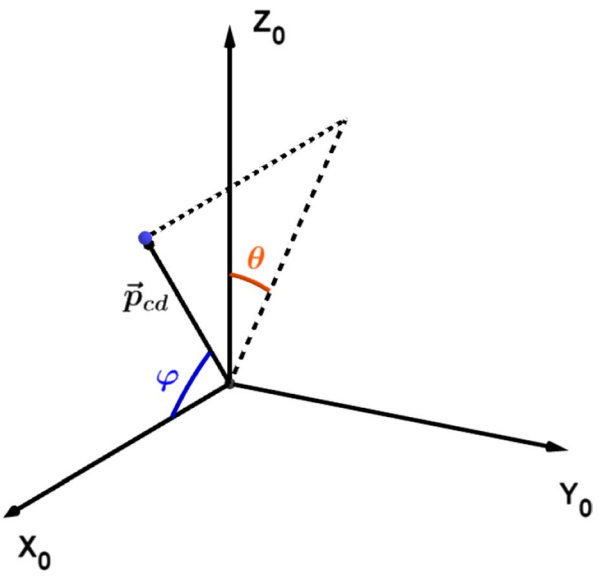

Fig. 5 Pseudo-inertial reference frame and definition of φ and θ coordinates

As has been said previously, the relative orientation between the satellites can be defined by a unitary vector centered in the origin and parallel to the relative position vector. To obtain a set of directions covering all the possible orientations, the HEALPix [10] scheme for tessellating the sky has been used, specifically, an implementation called astropy-healpix, an Astropy [14] coordinated package. This equal area scheme is based on the discretization of a sphere surface (see Fig. 6), providing a nearly regular grid which avoids distortions that appear when the coordinates φ and θ are discretized with equispaced points. HEALPix also allows to interpolate results in any point in the sphere using bilinear interpolation.

The numerical algorithm is focused on detecting the access to permit the later analysis of each one. The access event occurs when the line of sight between both satellites is inside the FoV of the chief instrument, which can be verified with the dot product between the orientation vector and the pointing direction of the

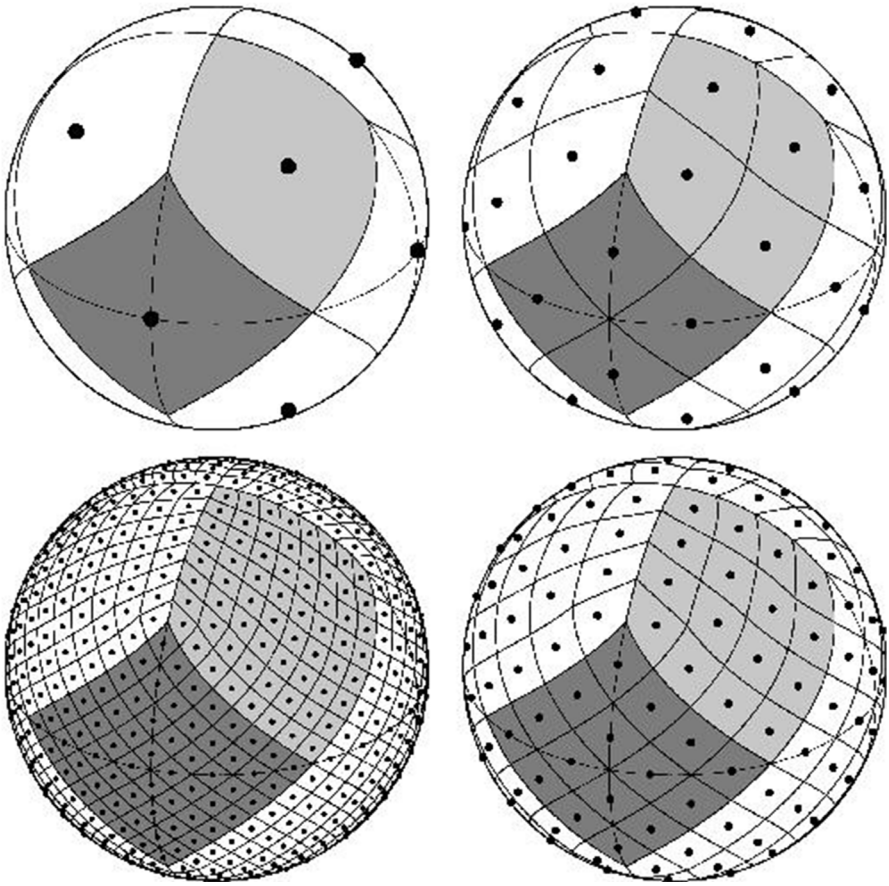

Fig. 6 Discretization of an sphere following HEALPix approach. From [10]

instrument. This is done at every step time for each orientation obtained from the discretization, computing the number of accesses and its duration. The simulations were performed using SciPy [19].

3 Access Analysis

In the following subsections, a set of parameters that describe the access features are studied.

3.1 Total Access Time

The first parameter to be analysed is the total access time (T_{total}) of an inertial direction in the sky. As mentioned in (10) this direction can be defined with its φ and θ coordinates. The total access time is defined as the total amount of time that the deputy, i.e., the direction that defines its relative position, stays inside the instrument FoV. It is a feature of a given scan strategy.

3.1.1 Analytical Approach for Total Access Time

As explained before, if the rotation times (T_{spin} and T_{prec}) are properly selected and the analysis time is long enough, it can be assumed that the results will be axial-symmetric. This implies that T_{total} will not depend on θ and only its variation with the φ coordinate of the direction is relevant. Thus, since T_{total} does not depend on θ, it will be equal for all the points in the sky with the same φ. Furthermore, the precession speed does not influence the fraction of time that each point of the sky is seen as any increase in the speed will shorten the access duration but it will also make the number of accesses grow proportionally. Therefore, an arbitrary precession speed case can be analysed and the conclusions about T_{total} will be applicable to other velocities as long as the high combined period condition is met.

The instrument direction over the time, $\mathbf{q}(t)$, can also be expressed in terms of φ and θ coordinates, however, as the final value of T_{total} does not depend on θ, only the variation of the angle between the direction of the instrument and the X_0-axis is relevant. This angle, called here φ_v, only depends on the spin motion and its variation is periodic every spin cycle, thus, the value of T_{total} obtained with the motion of the instrument, $\mathbf{q}(t)$, will be equivalent to the one obtained by a vertical periodic motion $\mathbf{q}^*(t)$ in the X_0Y_0-plane. Therefore, the analysis of this motion during one spin period will provide all the required information about T_{total}.

Based on these considerations, let us study how much time the directions with the same φ coordinate are inside the instrument FoV for the simplest possible

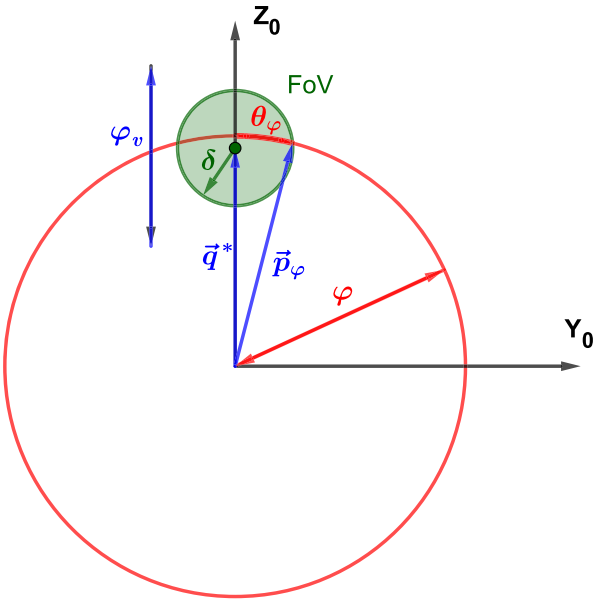

Fig. 7 Geometrical scheme for the simplified case considered. Note that $\mathbf{q}^*$ will move vertically as φ_v changes

case: the one with almost zero precession ($T_{prec} \longrightarrow \infty$). Furthermore, it is only necessary to study one spin cycle, which, as previously said, can be represented as a vertical periodic motion with $\varphi_v = f(t)$. A scheme of this analysis is shown in Fig. 7. It should be noticed that, although these schemes do not provide a rigorous projection of the trace, it helps to facilitate the understanding of the process. The angles regarding the precession axis are represented as in an azimuthal equidistant projection, i.e., directions with the same φ coordinate are displayed as a circumference with a radius proportional to φ.

In order to calculate $\varphi_v = f(t)$ it is necessary to define the direction of the instrument $\mathbf{q}$. This direction can be expressed as a rotation around spin axis $\mathbf{u}_{spin}$, which in this analysis is fixed and contained in X_0Z_0-plane, as follows

$$\mathbf{u}_{spin} = \begin{Bmatrix} \cos(\alpha) \\ 0 \\ \sin(\alpha) \end{Bmatrix}. \tag{11}$$

The rotation matrix around the direction defined by this vector is

$$R = \begin{bmatrix} c_\phi + c_\alpha^2(1-c_\phi) & -s_\alpha s_\phi & c_\alpha s_\alpha(1-c_\phi) \\ s_\alpha s_\phi & c_\phi & -c_\alpha s_\phi \\ c_\alpha s_\alpha(1-c_\phi) & c_\alpha s_\phi & c_\phi + s_\alpha^2(1-c_\phi) \end{bmatrix}, \tag{12}$$

where ϕ is the rotated angle. If the starting position of $\mathbf{q}$ is

$$\mathbf{q}_0 = \begin{Bmatrix} \cos(\alpha+\beta) \\ 0 \\ \sin(\alpha+\beta) \end{Bmatrix}, \tag{13}$$

also contained in X_0Z_0-plane, the value of $\mathbf{q}$ depending on the spin angle would be

$$\mathbf{q}(\phi) = R \cdot \mathbf{q}_0 = \begin{Bmatrix} \cos(\alpha)\cos(\beta) - \sin(\alpha)\sin(\beta)\cos(\phi) \\ -\sin(\beta)\sin(\phi) \\ \cos(\alpha)\sin(\beta)\cos(\phi) + \sin(\alpha)\cos(\beta) \end{Bmatrix}. \tag{14}$$

The angle between the instrument direction and the precession axis, φ_v, is then obtained from the dot product between $\mathbf{q}$ and X_0-axis direction as

$$\varphi_v = \arccos(\cos(\alpha)\cos(\beta) - \sin(\alpha)\sin(\beta)\cos(\phi)). \tag{15}$$

Then, the equivalent vertical motion of the instrument, $\mathbf{q}^*$, is given by

$$\mathbf{q}^* = \begin{Bmatrix} \cos(\varphi_v) \\ 0 \\ \sin(\varphi_v) \end{Bmatrix}, \tag{16}$$

where $\varphi_v(t)$ can be calculated using (15).

Once the motion of the instrument has been characterised, the next step is to calculate the fraction of the circumference inside the FoV in each instant. A generic point of the circumference, $\mathbf{p}$, is given by (10). The one where the access starts in a certain instant can be written as

$$\mathbf{p}_\varphi = \begin{Bmatrix} \cos(\varphi) \\ \sin(\varphi)\sin(\theta_\varphi) \\ \sin(\varphi)\cos(\theta_\varphi) \end{Bmatrix}. \tag{17}$$

For a given position $\mathbf{q}^*$ of an instrument with FoV half-angle δ, the vector of the instrument $\mathbf{q}^*$ will form an angle δ with $\mathbf{p}_\varphi$. Therefore

$$\mathbf{q}^* \cdot \mathbf{p}_\varphi = \cos(\delta). \tag{18}$$

From this equation, the half-arc angle θ_φ of points with the same φ that are inside the FoV (see Fig. 7) can be obtained

$$\cos(\theta_\varphi) = \frac{\cos(\delta) - \cos(\varphi_v)\cos(\varphi)}{\sin(\varphi_v)\sin(\varphi)}. \tag{19}$$

Therefore, the fraction of points inside the FoV is $2\theta_\varphi/2\pi$.

Averaging this fraction over a half spin period, the fraction of time that directions with the same φ spend inside the FoV during one period can be obtained. This averaged fraction is

$$f_t(\varphi) = \frac{1}{\pi}\int_0^{\pi} \frac{1}{\pi}\mathrm{Re}\left(\arccos\left(\frac{\cos(\delta)-\cos(\varphi_v)\cos(\varphi)}{\sin(\varphi_v)\sin(\varphi)}\right)d\phi\right), \tag{20}$$

as the second half of the period is symmetric to the first one.

The total access time for a point with angle φ can be calculated multiplying this fraction by the total time of analysis, T_{sim}

$$T_{total}(\varphi) = f_t(\varphi)\cdot T_{sim}. \tag{21}$$

As can be deduced from equations (15) and (20), f_t depends solely on φ, with α, β and δ as parameters while the spin and precession speeds do not appear. An example of the solution of $f_t(\varphi)$ is shown in Fig. 8.

3.1.2 Numerical Results for Total Access Time

The total access time has been calculated following the methodology explained in Sect. 2.1. To represent the numerical results, a Hammer projection [15] of the whole sphere has been chosen to depict them. The center of the image corresponds to the observation direction of the precession axis, while the lateral regions represent the opposite direction. The result for the same example on Fig. 8 is presented in Fig. 9, where the axial-symmetry is clear.

The main disadvantage of this approach is its computational cost, which grows proportionally with the simulation time and both the temporal and spatial discretization (nevertheless, more than one parameter can be calculated in the same simulation with small additional effort). For this reason, the analytical approach can be useful for validation of the numerical method. In Fig. 10 the analytical and

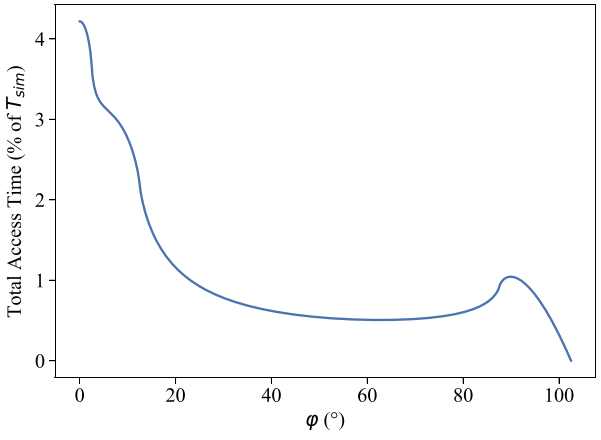

Fig. 8 Variation of the percentage of access time regarding the total time considered as a function of coordinate φ. Parameters considered: $T_{sim} = 1$ day, $\alpha = 45°$, $\beta = 50°$, $T_{spin} = 10$ min, $T_{prec} = 93$ min, and $\delta = 7.5°$

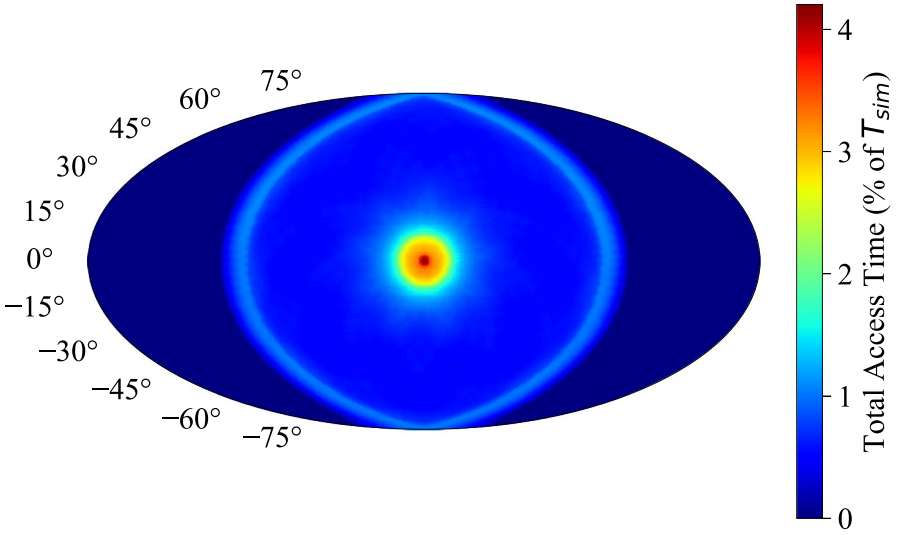

Fig. 9 Total access time. Parameters considered: $T_{sim} = 1$ day, $\alpha = 45°$, $\beta = 50°$, $T_{spin} = 10$ min, $T_{prec} = 93$ min, and $\delta = 7.5°$

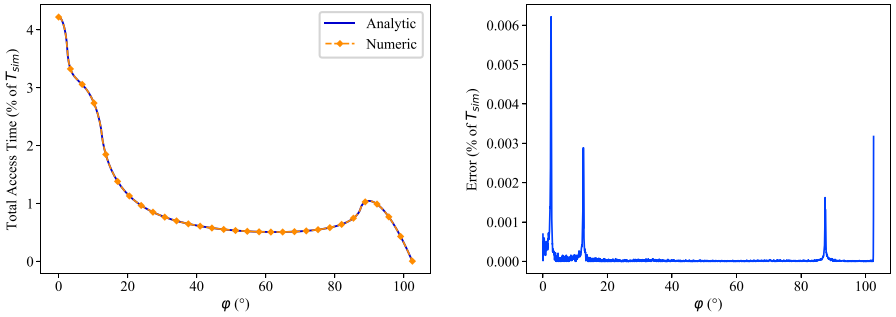

(a) Comparison. (b) Error.

Fig. 10 Comparison (**a**) and error (**b**) between the analytical and numerical results for the variation of the total access time as a function of coordinate φ. Parameters considered: $T_{sim} = 1$ day, $\alpha = 45°$, $\beta = 50°$, $T_{spin} = 10$ min, $T_{prec} = 93$ min, and $\delta = 7.5°$

numerical results for total access time are compared. The numerical results have been averaged over θ. Overall, the error is low except in the deep slope zones of the curve, due to the limited precision of the bilinear interpolation. The criterion to consider that both results coincide has been established in an RMSE (root-mean-square error) that is lower than 1E-3% of T_{sim}. This is fulfilled for all the scan strategies tested.

3.2 Mean Access Time

The mean access time, T_{mean}, can be defined as the total access time over a period of time divided by the number of accesses. As before, for a direction $\mathbf{p}$, if spin and precession are chosen properly, it is possible to assure that this parameter does not depend on θ.

3.2.1 Analytical Approach for Mean Access Time

In the previous section, the total access time has been obtained, and now the number of accesses is calculated following a similar approach. Although, for calculating the total access time the precession motion can be omitted, it will influence the number of accesses for a certain φ and it has to be taken into account if precession speed Ω is not negligible.

In order to calculate the number of accesses, it is not relevant how much time one given direction stays inside the FoV, but whether after one spin period it has been seen or not. Thus, the approach to solve the problem is to calculate the proportion of directions, f_m, with the same φ coordinate that have been inside the FoV after one spin period . As before, the motion is symmetrical with regard to the axis of rotation after a period, therefore, this proportion must remain constant for subsequent periods. If accesses are equally distributed along all the points with the same φ, the total number of accesses during a given period can be obtained by multiplying the number of spin cycles by the aforementioned proportion

$$N(\varphi) = f_m(\varphi)\frac{T_{sim}}{T_{spin}}. \tag{22}$$

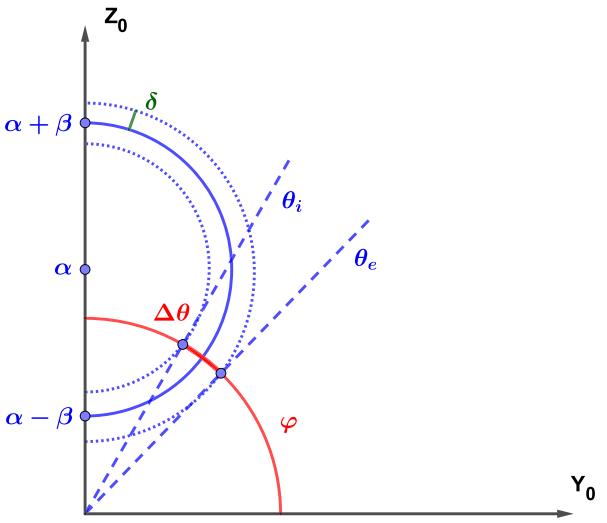

Fig. 11 Geometrical scheme for the mean access time when precession is negligible

First, the case for Ω negligible is presented and then it will be extended to the general case that takes into account the precession speed. A geometrical scheme of half spin period when Ω is negligible is shown in Fig. 11.

Every half spin period, an arc of $\Delta\theta$ is seen from the instrument. Over one spin, this makes a proportion of

$$f_m = \frac{2\Delta\theta}{2\pi}, \tag{23}$$

which is equal to the mean number of accesses for all the directions with the same φ coordinate. The value of $\Delta\theta$ can be obtained as

$$\Delta\theta = \theta_e - \theta_i, \tag{24}$$

where θ_e and θ_i are the limits of the highlighted arc in Fig. 11. If Ω is negligible, this arc is limited by the two circles of radius $\beta + \delta$ and $\beta - \delta$. Therefore, following the same approach that in (19), the limit values are

$$\theta_i|_\varphi = \mathrm{Re}\left(\arccos\left(\frac{\cos(\beta-\delta) - \cos(\alpha)\cos(\varphi)}{\sin(\alpha)\sin(\varphi)}\right)\right), \tag{25}$$

and

$$\theta_e|_\varphi = \mathrm{Re}\left(\arccos\left(\frac{\cos(\beta+\delta) - \cos(\alpha)\cos(\varphi)}{\sin(\alpha)\sin(\varphi)}\right)\right). \tag{26}$$

Once θ_e and θ_i are obtained, the distance $2\Delta\theta$ can be calculated and using (23) in (22), the number of accesses will be

$$N(\varphi) = \frac{2\Delta\theta}{2\pi}\frac{T_{sim}}{T_{spin}}. \tag{27}$$

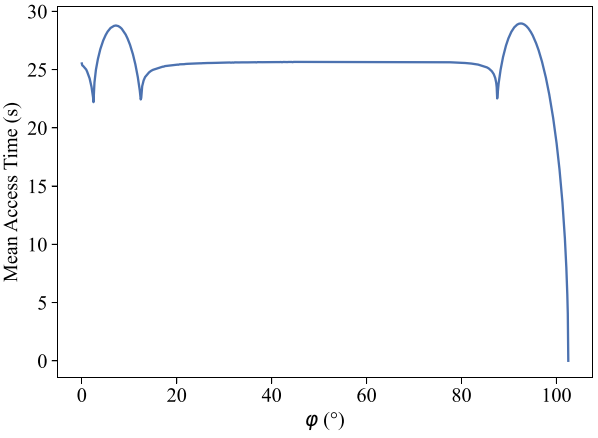

Fig. 12 Variation of the mean access time as a function of coordinate φ for negligible Ω. Parameters considered: $T_{sim} = 1$ day, $\alpha = 45°$, $\beta = 50°$, $T_{spin} = 10$ min, and $\delta = 7.5°$

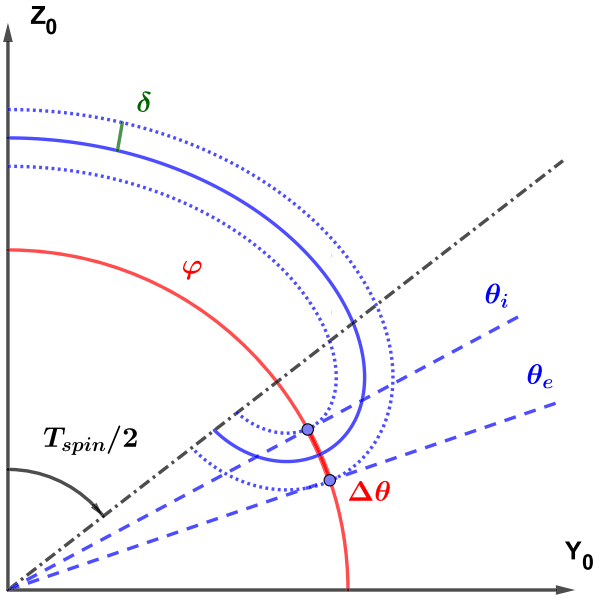

Fig. 13 Geometrical scheme for mean access time when precession speed is significant. Only the trace for half T_{spin} period is shown

Retrieving the total access time (21), the mean access time is

$$T_{mean}(\varphi) = \frac{T_{total}(\varphi)}{N(\varphi)} = T_{spin}\frac{f_t(\varphi)}{f_m(\varphi)}. \tag{28}$$

The mean access time profile for the case of negligible Ω is shown in Fig. 12.

However, if $\Omega < \omega$ but not negligible, the trace cannot be simplified as a circle. An example of how the scheme can look is shown in Fig. 13.

In this case, in order to calculate the value of θ_i and θ_e it is necessary to obtain the side curves of the trace. These curves are separated by a 2δ distance in the perpendicular direction to the trace. If the trace expression is $\mathbf{q}(t)$ (6), the equations of the exterior and interior curves are respectively

$$\mathbf{q}_e(t) = \mathbf{q}\cos(\delta) + \mathbf{n}\sin(\delta) = \begin{Bmatrix} x_e(t) \\ y_e(t) \\ z_e(t) \end{Bmatrix} \tag{29}$$

and

$$\mathbf{q}_i(t) = \mathbf{q}\cos(\delta) - \mathbf{n}\sin(\delta) = \begin{Bmatrix} x_i(t) \\ y_i(t) \\ z_i(t) \end{Bmatrix}. \tag{30}$$

with $\mathbf{n}$ being the unitary normal to the trace, whose expression is:

$$\mathbf{n} = \frac{\mathbf{q}'(t) \wedge \mathbf{q}(t)}{|\mathbf{q}'(t)|}. \tag{31}$$

It is more useful to express the external and internal curves in terms of its φ and θ components. These can be calculated from the Cartesian coordinates from (29) and (30) as

$$\varphi_e(t) = \mathrm{Re}(\arccos(y_e(t))) \tag{32}$$

$$\theta_e(t) = \mathrm{Re}\left(\arccos\left(\frac{z_e(t)}{\sin(\varphi_e(t))}\right)\right) \tag{33}$$

and

$$\varphi_i(t) = \mathrm{Re}(\arccos y_i(t)) \tag{34}$$

$$\theta_i(t) = \mathrm{Re}\left(\arccos\left(\frac{z_i(t)}{\sin(\varphi_i(t))}\right)\right). \tag{35}$$

With the equations of the external and internal curve, the procedure to calculate the $2\Delta\theta$ for a given φ is as follows: first, using equations (32) and (34) the instants t_i and t_e when the traces have respectively $\varphi_i = \varphi$ and $\varphi_e = \varphi$ are calculated. Second, these instants are used to calculate θ_e and θ_i with equations (33) and (35). Once these angles are obtained, the distance $2\Delta\theta$ can be determined and the number of accesses is obtained through equation (28). An example of the resulting profile obtained from equation (28) is shown in Fig. 14.

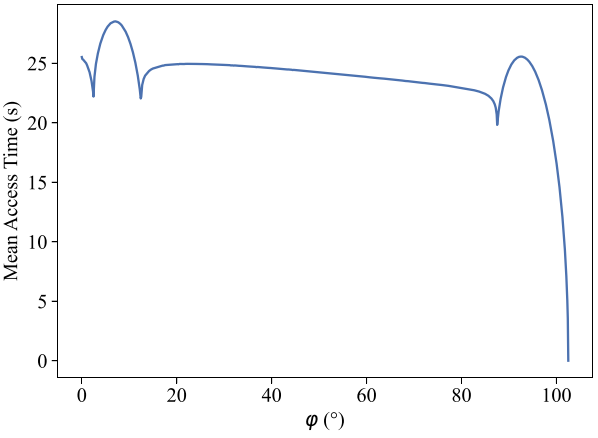

Fig. 14 Variation of the mean access time as a function of coordinate φ, with $\Omega < \omega$ but not negligible. Parameters considered: $T_{sim} = 1$ day, $\alpha = 45°$, $\beta = 50°$, $T_{spin} = 10$ min, $T_{prec} = 93$ min, and $\delta = 7.5°$

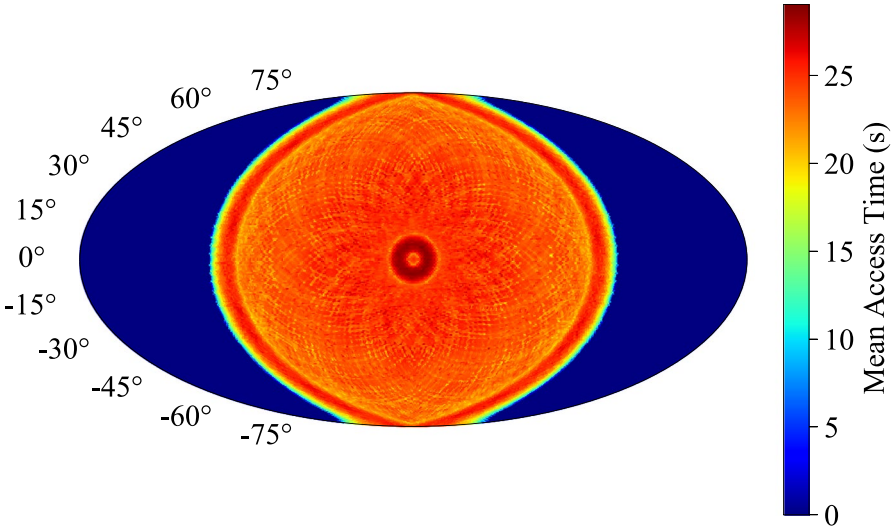

Fig. 15 Mean access time. Parameters considered: $T_{sim} = 1$ day, $\alpha = 45°$, $\beta = 50°$, $T_{spin} = 10$ min, $T_{prec} = 93$ min, and $\delta = 7.5°$

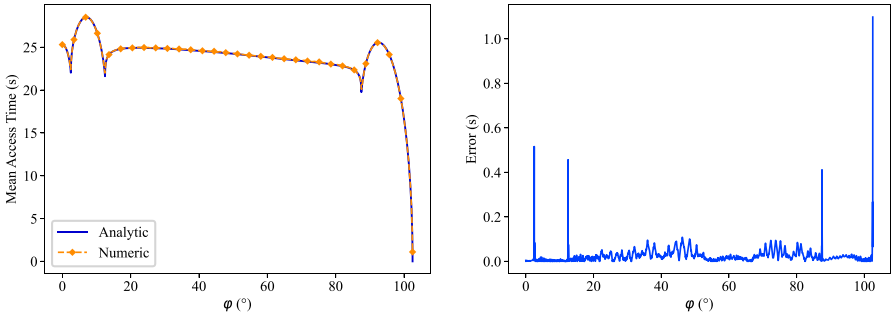

(a) Comparison. (b) Error.

Fig. 16 Comparison (**a**) and error (**b**) between the analytical and numerical results for the mean access time as a function of coordinate φ. Parameters considered: $T_{sim} = 1$ day, $\alpha = 45°$, $\beta = 50°$, $T_{spin} = 10$ min, $T_{prec} = 93$ min, and $\delta = 7.5°$

3.2.2 Numerical Results for the Mean Access Time

The numerical results for the mean access time for the same example on Fig. 14 are presented in Fig. 15. As can be seen, the mean access time also presents axial-symmetry.

In Fig. 16 the analytical and numerical results for mean access time are compared. The numerical results have been averaged over θ. In this case, the criterion to validate the results is that the RMSE is lower than the time step used for the numerical analysis. This is fulfilled for all the scan strategies tested.

3.3 Maximum Access Time

The maximum access time (T_{max}) is the maximum time that a direction $\mathbf{p} = \mathbf{f}(\varphi, \theta)$ can be inside the FoV of the instrument. This time also depends on the scan strategy and will not depend on θ if the rotation and precession are chosen properly.

3.3.1 Analytical Approach for Maximum Access Time

For the maximum access time, the procedure followed is similar to the mean access time section. First, the expression for the duration of an access with no precession motion is obtained. But now, the maximum access time is studied instead of the mean access time. Then, the precession motion is added, distinguishing two cases according to whether the precession speed is negligible or not, like in the mean access time section.

First, the case without precession will be analyzed. As there is only rotation around the spin axis, the motion will be analyzed centered in that axis, the new coordinates being θ^* and φ^*. Furthermore, in order to obtain the access time for this pure spin motion, it is advantageous to consider that the instrument remains fixed and it is the direction vector the one that rotates around the spin axis (X^* in the new coordinates). Without loss of generality, it is assumed that the instrument is located on the X^*Z^*-plane, separated by an angle β from the spin axis, as shown in Fig. 17, thus,

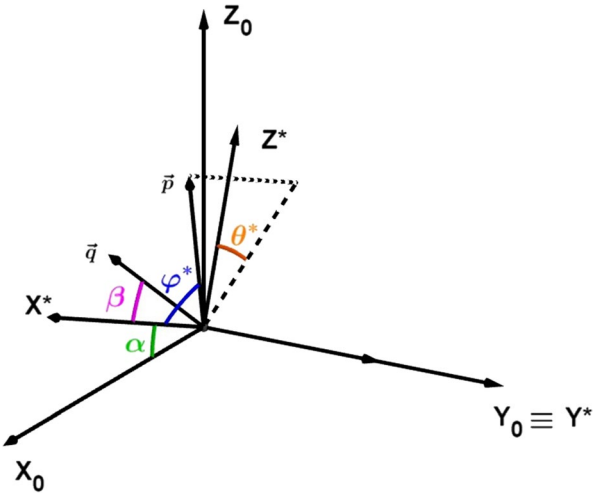

Fig. 17 New reference system defined

$$\mathbf{q} = \begin{Bmatrix} \cos\beta \\ 0 \\ \sin\beta \end{Bmatrix}. \tag{36}$$

In this new frame, the direction vector (37) is separated an angle φ^* from the spin axis, and its projection over the Y^*Z^*-plane form an angle θ^* with the Z^*-axis, so it can be expressed as

$$\mathbf{p} = \begin{Bmatrix} \cos(\varphi^*) \\ \sin(\varphi^*)\sin(\theta^*) \\ \sin(\varphi^*)\cos(\theta^*) \end{Bmatrix}. \tag{37}$$

The starting condition of an access (18) establishes that the relation between β, θ^*, φ^* and δ for a given instant is

$$\cos(\theta^*_\varphi) = \frac{\cos(\delta) - \cos(\varphi_v)\cos(\varphi^*)}{\sin(\varphi_v)\sin(\varphi^*)}. \tag{38}$$

This equation is similar to (19). Due to how the direction vector is expressed, the angle θ^*_φ is the half-arc of its trajectory inside the FoV. Therefore, if the trajectory in one spin period has a length of 2π, the proportion of time inside the FoV is $2\theta^*_\varphi/2\pi$ and the access time is

$$T_{access} = \frac{T_{spin}}{\pi}\mathrm{Re}\left(\arccos\left(\frac{\cos(\delta) - \cos(\beta)\cos(\varphi^*)}{\sin(\beta)\sin(\varphi^*)}\right)\right). \tag{39}$$

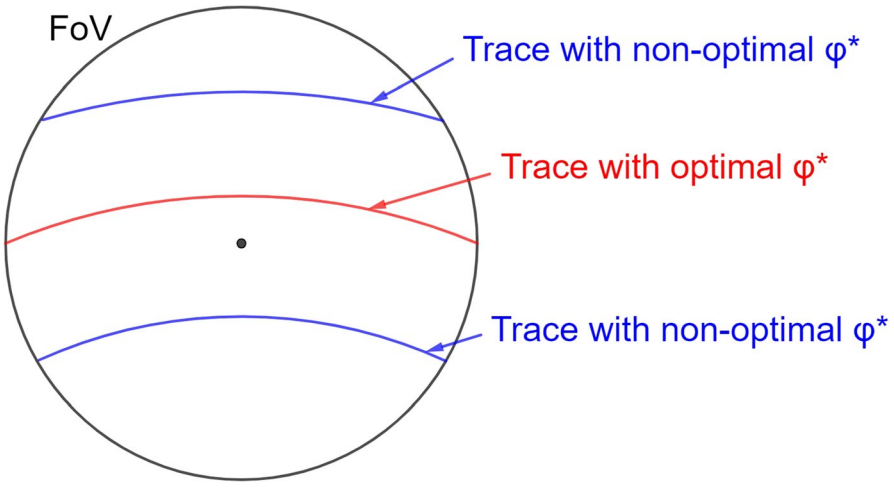

Fig. 18 Trace of the direction vector over the FoV for different φ^* coordinates

The maximum access time can be obtained deriving (39) with regard to φ^* and equating to zero, which gives

$$t_{max} = \frac{T_{spin}}{\pi}\mathrm{Re}\left(\arccos\left(\frac{\sqrt{\cos^2(\delta)-\cos^2(\beta)}}{\sin(\beta)}\right)\right). \tag{40}$$

This maximum access time, called here optimum access time, is achieved for the directions whose φ^* coordinate is equal to $\varphi^*_{t_{max}}$, whose value is

$$\varphi^*_{t_{max}} = \arctan\left(\frac{\sqrt{\cos^2(\delta)-\cos^2(\beta)}}{\cos(\beta)}\right). \tag{41}$$

For any higher or lower value of φ^*, the access time will be lower than the optimum access time. In Fig. 18 it is shown a scheme of this behaviour.

As mentioned before, to add the effect of precession, two cases have been considered. For the case where $\Omega << \omega$, i.e., the precession motion is much slower than the spin motion, it can be assumed that the trace of the instrument over the sky is nearly a circumference and therefore the previous results can be used directly. As the spin axis rotates around the precession axis, those points in the sky which, at any time, are at an angular distance of $\varphi^*_{t_{max}}$ will have an optimum access time. For any point with $\varphi < \alpha + \varphi^*_{t_{max}}$ and $\varphi > |\alpha - \varphi^*_{t_{max}}|$ there will be an instant in which the trace is at the right point. Therefore, its maximum access time will be the optimum access time.

For those directions whose φ coordinate is out of the aforementioned range, the maximum access time will not be the optimum. However, (39) is still valid assuming that $\varphi^* = \alpha - \varphi \cdot \mathrm{sgn}(\alpha - \varphi^*_{t_{max}})$ for $\varphi < |\alpha - \varphi^*_{t_{max}}|$ and $\varphi^* = \varphi - \alpha$ for $\varphi > \alpha + \varphi^*_{t_{max}}$. Taking all of this into account, according to the value of φ, its maximum access time is

for $0 < \varphi < |\alpha - \varphi^*_{t_{max}}|$:

$$t_1 = \frac{T_{spin}}{\pi}\mathrm{Re}\left(\arccos\left(\frac{\cos(\delta)-\cos(\beta)\cos(\alpha-\varphi\cdot\mathrm{sgn}(\varphi^*_{t_{max}}))}{\sin(\beta)\sin(\alpha-\varphi\cdot\mathrm{sgn}(\varphi^*_{t_{max}}))}\right)\right) \tag{42}$$

for $|\alpha - \varphi^*_{t_{max}}| < \varphi < \alpha + \varphi^*_{t_{max}}$:

$$t_2 = t_{max} = \frac{T_{spin}}{\pi}\mathrm{Re}\left(\arccos\left(\frac{\sqrt{\cos^2(\delta)-\cos^2(\beta)}}{\sin(\beta)}\right)\right) \tag{43}$$

for $\alpha + \varphi^*_{t_{max}} < \varphi < \pi$:

$$t_3 = \frac{T_{spin}}{\pi}\mathrm{Re}\left(\arccos\left(\frac{\cos(\delta)-\cos(\beta)\cos(\varphi-\alpha)}{\sin(\beta)\sin(\varphi-\alpha)}\right)\right) \tag{44}$$

An example of the maximum access time profile in the case of negligible Ω is shown in Fig. 19. The three regions can be clearly identified. For the central region, the maximum access time is the highest and is constant.

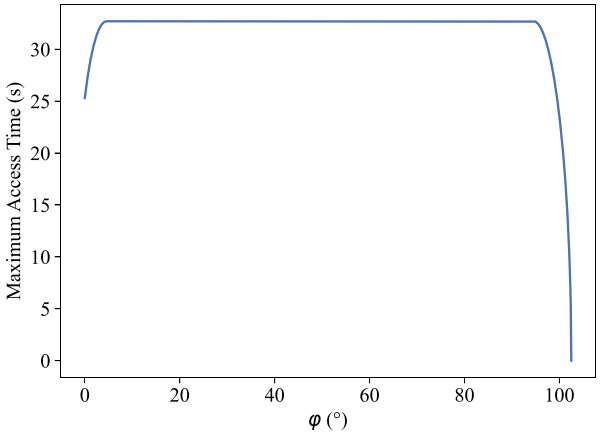

Fig. 19 Variation of the maximum access time as a function of coordinate φ for Ω negligible. Parameters considered: $T_{sim} = 1$ day, $\alpha = 45°$, $\beta = 50°$, $T_{spin} = 10$ min, and $\delta = 7.5°$

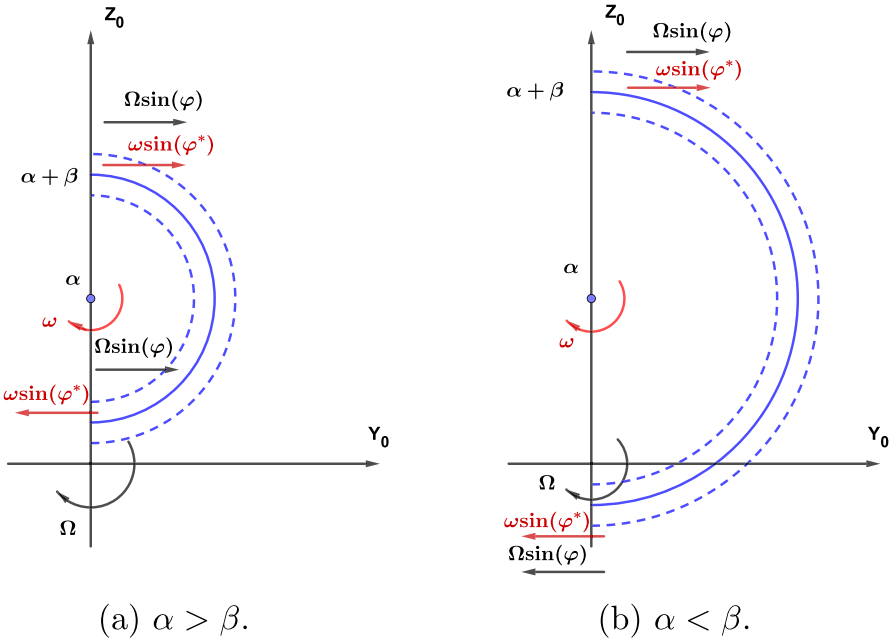

Fig. 20 Scheme of how the precession speed Ω (black) would be added or subtracted to spin speed ω (red) according to whether $\alpha > \beta$ or $\alpha < \beta$

For the case of a significant precession speed, no analytical solution has been found. However, its effect can be approximated by modifying the maximum access times (42), (43) and (44).

First, lets analyze the points that do not reach $\varphi^*_{t_{max}}$ and therefore, t_{max}. These points have their own optimum access time when they reach the minimum angular distance from the spin axis. If the precession motion is taken as a rotation of

the sky instead of the instrument, it can be assumed that the access time will increase or decrease, according to whether such rotation has the opposite or the same direction as the spin rotation. A scheme explaining this behavior is shown in Fig. 20. When $\alpha > \beta$, as the speed grows the maximum access time decreases for large values of φ and increases for small values of φ. In the other case, $\alpha < \beta$, the maximum access time will be smaller for any value of φ, as the speed with which the direction travels across the FoV is always increased by the precession motion.

Therefore, it is possible to approximate how the maximum access time changes introducing a scaling factor for t_1 and t_3 as follows

for $0 < \varphi < |\alpha - \varphi^*_{t_{max}}|$:

$$t_1^* = t_1 \frac{\omega \sin(\alpha - \varphi k)}{\omega \sin(\alpha - \varphi k) - \Omega \sin(\varphi k)} \tag{45}$$

for $\alpha + \varphi^*_{t_{max}} < \varphi < \pi$:

$$t_3^* = t_3 \frac{\omega \sin(\varphi - \alpha)}{\omega \sin(\varphi - \alpha) + \Omega \sin(\varphi)} \tag{46}$$

with $k = \text{sgn}(\alpha - \beta)$. The smaller the values of δ and Ω are, the more accurate these approximations will be.

For t_2, the proposed approach is as follows. Taking into account that the instrument sweep speed is produced both by spin and precession, assuming that δ is small and the precession motion slow, it is reasonable to expect that the component of the precession motion parallel to the spin speed component will be the more significant one in changing the access time. Thus, t_2 can be scaled similarly to t_1 and t_3 but this time with the component of precession speed parallel to spin speed

for $|\alpha - \varphi^*_{t_{max}}| < \varphi < \alpha + \varphi^*_{t_{max}}$:

$$t_2^* = t_2 \frac{\omega \sin(\varphi^*_{t_{max}})}{\omega \sin(\varphi^*_{t_{max}}) + \Omega \sin(\varphi)\gamma} \tag{47}$$

where γ is the projection of the precession velocity unitary vector (Fig. 21), $\mathbf{v}_{prec}$, over the spin velocity unitary vector, $\mathbf{v}_{spin}$. To obtain this value, first the vector $\mathbf{v}_{spin}$ is calculated, tangent to the spin velocity. In order to do that, (14) is derived with regard to ϕ

$$\frac{d\mathbf{q}}{d\phi} = \begin{Bmatrix} \sin(\alpha)\sin(\beta)\sin(\phi) \\ \sin(\beta)\cos(\phi) \\ -\cos(\alpha)\sin(\beta)\sin(\phi) \end{Bmatrix}, \tag{48}$$

and then normalized

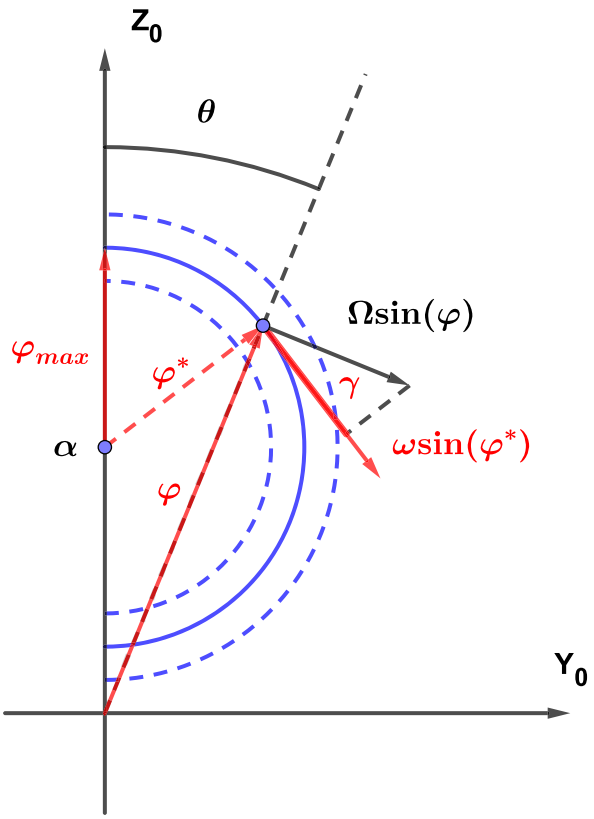

Fig. 21 Definition of γ, projecting the precession velocity vector over the spin velocity vector

$$\mathbf{v}_{spin} = \frac{d\mathbf{q}/d\phi}{|d\mathbf{q}/d\phi|} = \begin{Bmatrix} \sin(\alpha)\sin(\phi) \\ \cos(\phi) \\ -\cos(\alpha)\sin(\phi) \end{Bmatrix} \tag{49}$$

The vector tangent to the precession velocity, $\mathbf{v}_{prec}$, can be easily expressed as a function of the τ angle, which is defined in Fig. 22

$$\mathbf{v}_{prec} = \begin{Bmatrix} \cos(\tau) \\ 0 \\ -\sin(\tau) \end{Bmatrix}. \tag{50}$$

The relation between both angles is

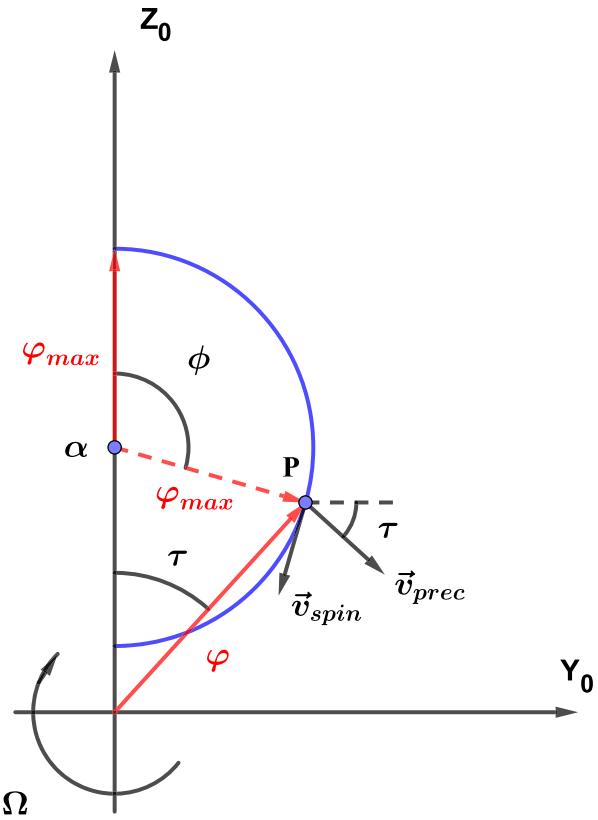

Fig. 22 Geometrical scheme of the approach followed to obtain γ

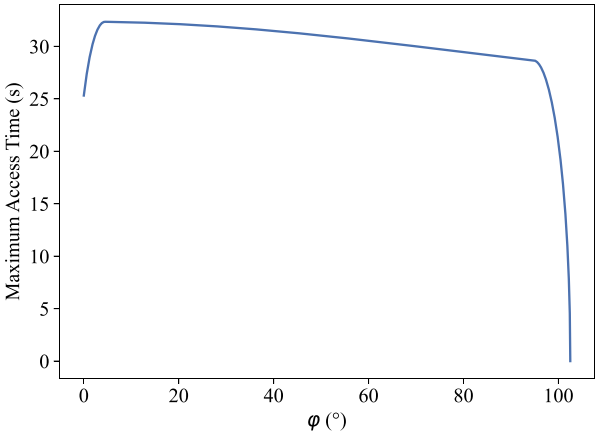

Fig. 23 Variation of the maximum access time as a function of coordinate φ for a non-negligible Ω. Parameters considered: $T_{sim} = 1$ day, $\alpha = 45°$, $\beta = 50°$, $T_{spin} = 10$ min, $T_{prec} = 93$ min, and $\delta = 7.5°$

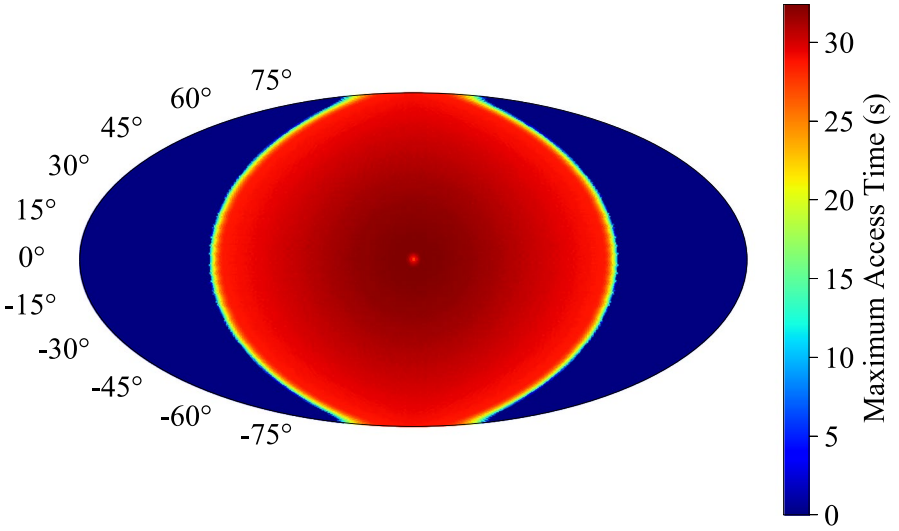

Fig. 24 Maximum access time. Parameters considered: $T_{sim} = 1$ day, $\alpha = 45°$, $\beta = 50°$, $T_{spin} = 10$ min, and $\delta = 7.5°$

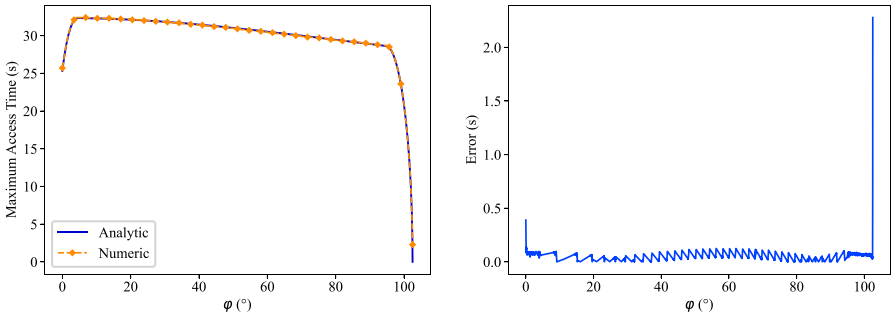

(a) Comparison. (b) Error.

Fig. 25 Comparison (**a**) and error (**b**) between the analytical and numerical results for the maximum access time as a function of coordinate φ. Parameters considered: $T_{sim} = 1$ day, $\alpha = 45°$, $\beta = 50°$, $T_{spin} = 10$ min, and $\delta = 7.5°$

$$\tau = \arctan\left(\frac{\sin(\varphi^*_{t_{max}})\sin(\phi)}{\cos(\alpha)\sin(\varphi^*_{t_{max}})\cos(\phi) + \sin(\alpha)\cos(\varphi^*_{t_{max}})}\right). \tag{51}$$

Then, projecting $\mathbf{v}_{prec}$ over $\mathbf{v}_{spin}$, γ is obtained

$$\gamma = \cos(\phi)\cos(\tau) + \cos(\alpha)\sin(\phi)\sin(\tau), \tag{52}$$

where ϕ can be expressed as a function of φ, $\varphi^*_{t_{max}}$, and α, as follows

$$\phi = \arccos\left(\frac{\cos(\alpha)\cos(\varphi^*_{t_{max}}) - \cos(\varphi)}{\sin(\alpha)\sin(\varphi^*_{t_{max}})}\right). \tag{53}$$

In Fig. 23 an example of the resulting profile obtained from equations (45), (46) and (47) is shown.

3.3.2 Numerical Results for the Maximum Access Time

The numerical results for maximum access time for the same example given in Fig. 23 are presented in Fig. 24. As can be seen, this last parameter also presents axial-symmetry.

The analytical and numerical results for maximum access time are compared in Fig. 25. The numerical results have been averaged over θ. The same RMSE criterion as with T_{mean} has been used and it has been fulfilled for all the scan strategies tested.

4 Analysis of Viewed Detectors

The previous results have been obtained considering the whole instrument FoV. However, in a real instrument, the calibration signal would be received by the detectors distributed in the instrument focal plane. In the case of CMB telescopes, bolometers are used as detectors. This type of sensor measures the power of incident electromagnetic radiation and can be used in pairs to measure the polarization. In order to evaluate the performance of the calibration at detector level, it is necessary to model the instrument and how the signal arrives at the detectors. Such performance will be evaluated in terms of number of detectors reached by the calibration signal and whether they receive it at different angles.

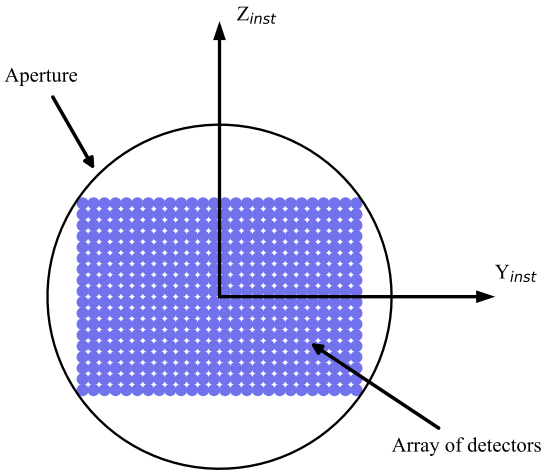

Fig. 26 Layout of the array of detectors

The obtention of analytical expressions for the quantities characterizing the access time has been based on a set of assumptions that simplify the problem, allowing the analytic treatment of the equations. Conversely, the inclusion of a detector distribution model increases the complexity of the problem and thus the use of numerical methods has been preferred. Two main aspects of the detectors have been analysed: the percentage of viewed detectors (ρ), which is affected by the number, angular size and distribution of the detectors; and the angular coverage parameter ($G(\xi)$), defined in the following section, and which indicates whether the reference signal reaches the detectors with a different polarization orientation during the calibration process.

4.1 Detectors and Signal Polarization Models

The instrument model consists of two elements: the instrument frame, whose attitude calculation has been already explained, and the detectors array geometry. The detectors array is a virtual representation of the instrument sensors layout. The sensors are located on the $Y_{inst}Z_{inst}$-plane of the instrument frame and modelled as a rectangular array (26x18) of equally sized circular detectors circumscribed by a circle that represents the resolution of the instrument, as depicted in Fig. 26. The total number of detectors is 468, with a half-angle resolution of 0.2° each one. The number of detectors is similar to that of the Low Frequency Telescope of future LiteBIRD mission [12], which has also a rectangular geometry.

The signal source of the calibration satellite is considered to be a point source in the space and the signal is assumed to arrive at the instrument as parallel rays. The assumption of parallel rays will be valid as long as the distance between the source and the observer is larger than the Fraunhofer distance, i.e., the observer is located in the far field of the source

$$d > \frac{2D}{\lambda}, \tag{54}$$

where d is the distance between source and observer, D is the instrument aperture and λ the wavelength of the signal. The source of the calibration signals has a size of a few centimeters ($D \sim 10^{-2}$ m) while the frequency is between 40 GHz and 400 GHz for the case considered in this work ($\lambda \sim 1$ mm). Therefore, the minimum distance between the source and the instrument should be roughly tens of meters.

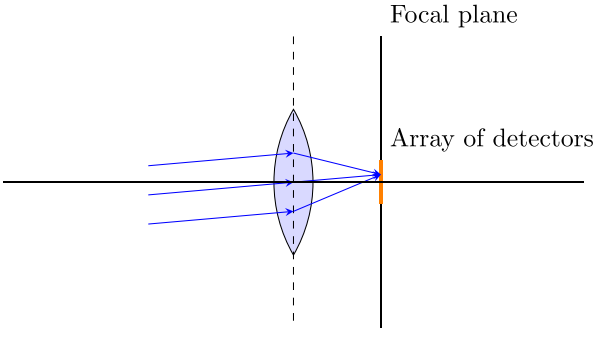

Fig. 27 Simplified optical model considered. Each possible direction within the FoV maps one unique point in the focal plane

The particularities of the telescope optics are omitted and it has been considered that the signal goes through a simple focusing lens [1, 12], thus, parallel rays arriving at the lens will converge to a unique point in the instrument focal plane, which is considered to be in the $Y_{inst}Z_{inst}$-plane of the instrument frame, where the array of detectors (see Fig. 27) is situated. Thus, each possible direction in the FoV corresponds unequivocally to a point in the circle where the array of detectors is circumscribed. This mapping is done projecting the orientation vector (equivalent to the incoming direction of the calibration signal) to the $Y_{inst}Z_{inst}$-plane.

The linear polarization of the signal can be defined by a vector perpendicular to the direction of propagation. In this case, the direction of propagation coincides with the LoS and the polarization of the calibration signal is chosen as an arbitrary direction perpendicular to the LoS. During the calibration, it is expected that the reference signal reaches the detectors several times. This will benefit the calibration process, particularly if the relative orientation between the polarization signal and the detectors framework of each measurement is different [5]. In order to assess if the signal arrives with different orientation, the parameter $G(\xi)$, derived from the one used in [4] to asses the angular coverage of each point in the sky, is defined for each of the N detectors which are reached by the reference signal at least once ($k \geq 1$)

$$G_j(\xi) = \left(\frac{1}{k} \sum_{i=1}^{k} \cos(2\xi_i) \right)^2 + \left(\frac{1}{k} \sum_{i=1}^{k} \sin(2\xi_i) \right)^2 \qquad \text{for } j = 1, \ldots, N \tag{55}$$

This parameter is computed for each detector using its measurements of the polarization (ξ_i), which is constant during the simulation, and then the mean value between all viewed detectors is calculated. If a detector is reached by the signal only once or several times but with similar orientation (or parallel), the $G(\xi)$ parameter will be equal or close to 1. Conversely, several measures with roughly perpendicular orientations will bring the parameter close to 0.

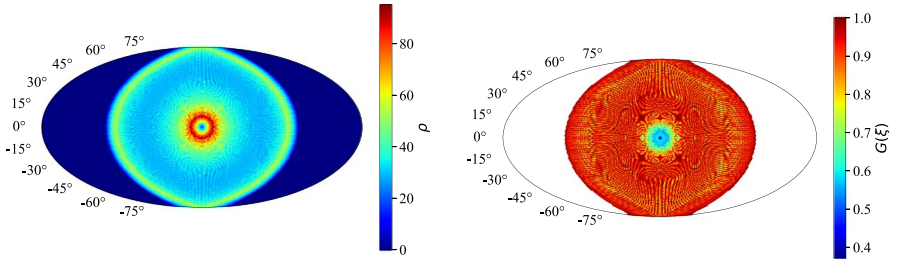

(a) ρ parameter. (b) $G(\xi)$ parameter.

Fig. 28 Numerical results for the percentage of viewed detectors and the $G(\xi)$ parameter. Parameters considered: $T_{sim} = 1$ day, $\alpha = 45°$, $\beta = 50°$, $T_{spin} = 10$ min, $T_{prec} = 93$ min, and $\delta = 7.5°$

4.2 Numerical Results of Detectors Analysis

Once the events have been detected, they are analyzed in detail. The percentage of viewed detectors (ρ) is obtained similarly to the access detection. For each access, it is checked which detectors receive the signal. These data can be further processed to obtain how many times the detectors are illuminated and for how long. The followed approach assumes that only one detector is illuminated simultaneously.

Additionally, the polarization of the arriving signal is computed and stored. After considering all of the time period, the parameter $G(\xi)$ is computed. This process is done for all the directions obtained in the discretization. In Fig. 28 the results for $T_{sim} = 1$ day are shown. As in the accesses analysis, both results present axial-symmetry. It can be observed that for relative angles between 10° and 15° degrees the majority of the detectors (around 80%) are reached and with different polarization orientation ($G(\xi)$ around 0.5). These results will be discussed in more detail in Sect. 5.

5 Application Example

In this section, the above methodology is applied to an example mission, showing how it can be used to select the best location to place a calibration satellite or to vary the scan strategy in order to obtain a better calibration performance. The baseline scan strategy has been chosen to be similar to those employed in previous and future CMB missions [6, 7, 11, 12, 17]: $\alpha = 45°$, $\beta = 50°$, $T_{spin} = 10$ min, $T_{prec} = 93$ min, and $\delta = 7.5°$. The detectors geometrical configuration used is the same as in Sect. 4.1. Unless otherwise stated, these results correspond to a simulation period of 1 day. This condition has been selected considering that the calibration process should not last longer to limit interference in the chief's observations.

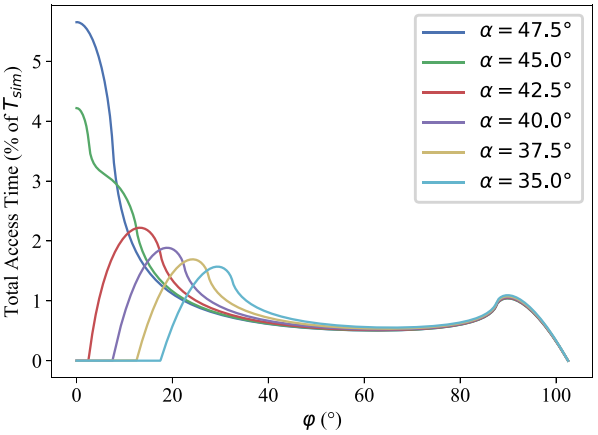

Fig. 29 Variation of the total access time as a function of coordinate φ for different values of α parameter. In all cases $\alpha + \beta = 95°$. Parameters considered: $T_{sim} = 1$ day, $T_{spin} = 10$ min, $T_{prec} = 93$ min and $\delta = 7.5°$

As shown in Equation (21), the total access time is proportional to the period of time considered (T_{sim}). The total access time will be a fraction of the period that is defined by (20). This will be the fraction of time available for calibration and it is presented in Fig. 8. The percentage of total access time has significantly higher values in the region near the precession axis, where it reaches roughly 4% and then descends steeply, remaining around 0.5% until it reaches the border, when it increases to 1% before becoming zero. This behaviour is due to the trace geometry. As is shown in Fig. 2, in the region around the precession axis and the border, the trace overlaps more than in the intermediate regions. This translates into accesses happening more frequently.

This dependency on the trace geometry is shown in equation (20), where only the scan strategy parameters α and β are present. The instrument FoV half-angle (δ) is also present, as it will affect the length of the accesses. However, it has been assumed as fixed. None of the attitude motion periods are present as their variations will cause no effect on the total access time. To show the effect of varying α and β, a parametric sweep has been carried out, with the constraint $\alpha + \beta = 95°$. Such constraint is established so that the whole sky is observed, ensuring that the instrument never points at the Sun. As shown in Fig. 29, the maximum value is always near $\varphi = |\alpha - \beta|$, reaching its highest value when $\alpha = \beta$, which means that the trace crosses exactly the precession axis in each spin cycle. As α decreases, so does the maximum value until a region with no access time emerges around the precession axis. The effect of decreasing β is symmetrical. That means, from the total access time point of view, a solution with $\alpha = X$ and $\beta = 95° - X$ is equal to a solution with $\beta = X$ and $\alpha = 95° - X$.

In Fig. 30 the mean access time and the maximum access time are compared. Neither of the two quantities depends on the period of time considered and they are rather uniform along φ coordinate. This can be seen from the mean access time in Equation (28), where T_{sim} disappears when dividing T_{total} by $N(\varphi)$. For the maximum access time, T_{sim} is not even considered in the approach followed to obtain its analytical expression. It should be noted that although these parameters do not depend

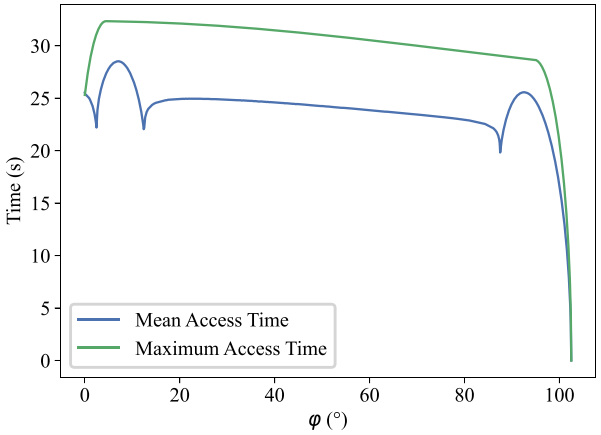

Fig. 30 Comparison between the variation of T_{mean} and the variation of T_{max} as functions of coordinate φ

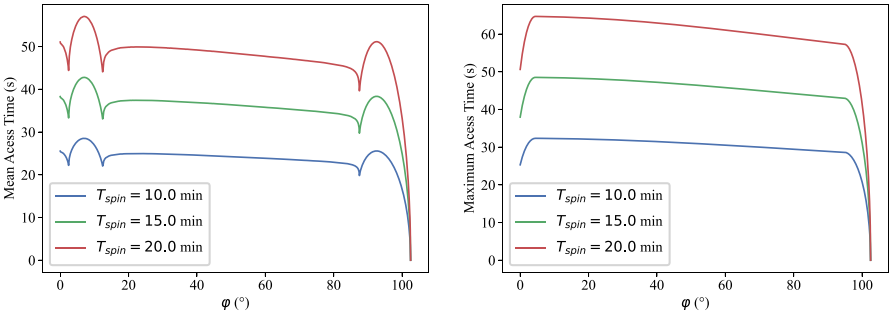

(a) Mean access time. (b) Maximum access time.

Fig. 31 Variation of T_{mean} and T_{max} as functions of coordinate φ for different values of the T_{spin} parameter

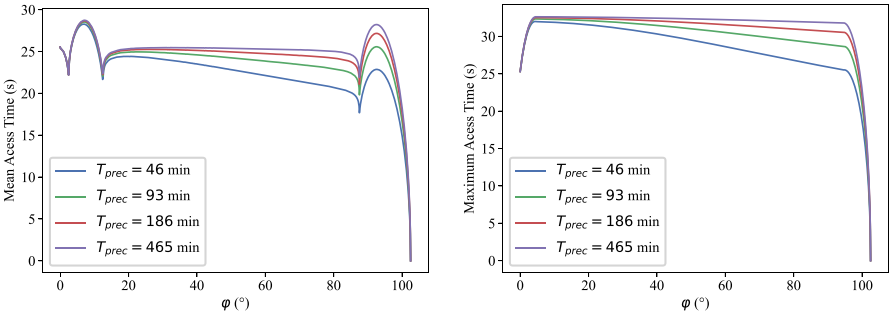

(a) Mean access time. (b) Maximum access time.

Fig. 32 Variation of T_{mean} and T_{max} as functions of coordinate φ for different values of the T_{prec} parameter

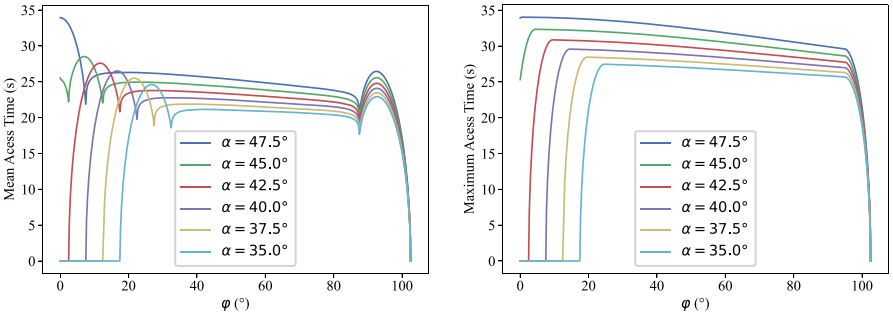

(a) Mean access time. (b) Maximum access time.

Fig. 33 Variation of T_{mean} and T_{max} as functions of coordinate φ for different values of α

on T_{sim}, it has been assumed that T_{sim} is large enough to achieve axial-symmetry in the results.

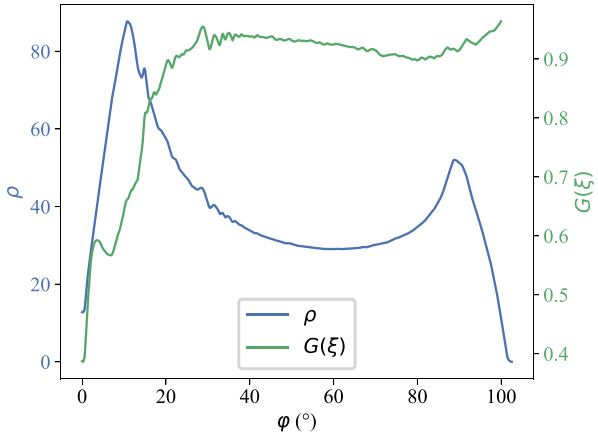

Fig. 34 Comparison between the variation of ρ and the variation of $G(\xi)$ as functions of coordinate φ

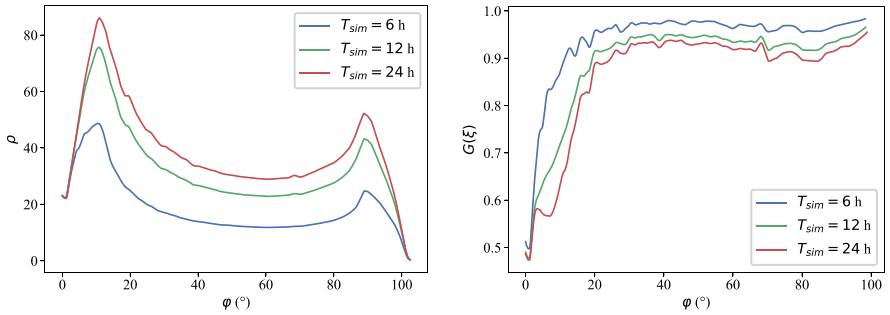

(a) ρ parameter. (b) $G(\xi)$ parameter.

Fig. 35 Variation of ρ and $G(\xi)$ as functions of coordinate φ for different values of T_{sim}

The period of spin motion will have a direct effect on both parameters since, as shown in equations (28), (45), (47) and (46), they scale proportionally to it, as shown in Fig. 31. In comparison, the precession period has little effect, being responsible for the slight negative slope as φ increases. As T_{prec} grows, this slope becomes steeper (Fig. 32).

As for the effect of varying α and β, the outcome is similar to that experienced by the total access time. Decreasing α reduces the value of the parameters in general and the no-access-zone emerges in the precession axis. This effect is shown in Fig. 33.

The results for ρ and $G(\xi)$ are shown in Fig. 34. The percentage of viewed detectors presents two maximums, the higher being close to the precession axis and the lower near the border. The $G(\xi)$ parameter has a different behaviour. Its lower point is in the precession axis, from where it raises steeply, staying close to 1. Although the most suitable regions of both parameters are close to the precession axis, they have very different behaviours since the maximum of ρ occurs during the steep change of $G(\xi)$ where a slight variation of φ has a significant effect on this parameter.

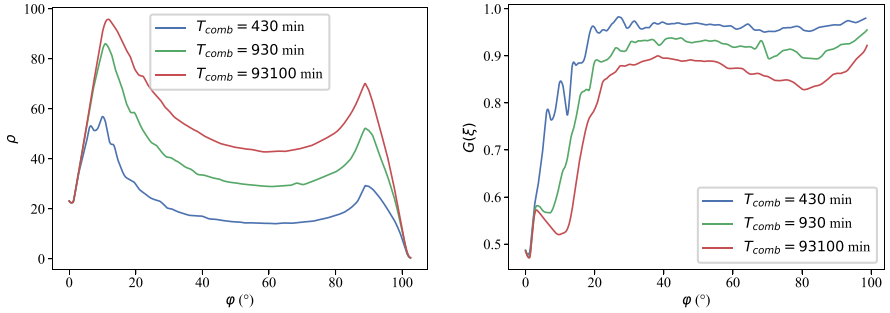

(a) ρ parameter. (b) $G(\xi)$ parameter.

Fig. 36 Variation of ρ and $G(\xi)$ as functions of coordinate φ for different values of T_{comb}, which are achieved keeping T_{spin} constant and using a T_{prec} of 90 min, 93 min and 93.1 min for T_{comb} cases of 430 min, 930 min and 93100 min, respectively

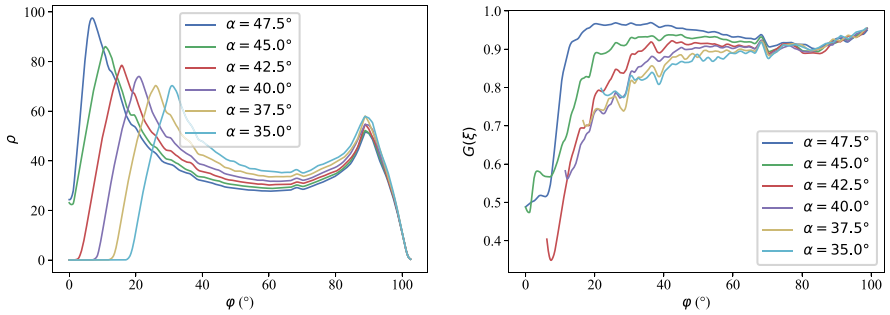

(a) ρ parameter. (b) $G(\xi)$ parameter.

Fig. 37 Variation of ρ and $G(\xi)$ as functions of coordinate φ for different values of α

Both parameters are mainly and similarly affected by T_{sim} and T_{comb}. As shown in Fig. 35(a), when T_{sim} increases, the percentage of viewed detectors grows for all values except for $\varphi = 0°$, where it remains constant. In this particular position, the trace of the deputy over the instrument is repeated in each access, so the same detectors are viewed each time, causing ρ to stay constant independently of T_{sim}. The same happens with $G(\xi)$ (Fig. 35(b)), increasing T_{sim} improves its value for all of the interval.

The spin and precession periods influence ρ and $G(\xi)$ through how they change T_{comb}. Slight variations in T_{prec} and T_{spin} change radically T_{comb}, which have a significant impact on ρ and $G(\xi)$. This behaviour is shown in Fig. 36. A variation of roughly 3 minutes in the precession period while keeping T_{spin} fixed causes very different results on both parameters. The higher the value of T_{comb}, the better coverage of all detectors.

Lastly, the variation of α and β also impact ρ and $G(\xi)$ (see Fig. 37). In the no-access-zone near the precession axis for a low α, the value of ρ drops to zero and $G(\xi)$ is not defined. As for T_{total}, the point of maximum percentage of viewed

detectors is displaced and its value reduced although the value is increased in general. An additional zone with $\rho = 0$ appears at the border. This occurs because for those conditions, the deputy crosses the instrument FoV in the lateral gaps that lie between the detectors array and the FoV border (Fig. 26). This behaviour is also experienced by $G(\xi)$ although in this case it is reduced in general when α decreases while its minimum value increases.

5.1 Discussion of Results

The results calculated above can be used to propose suitable locations for a calibration satellite and to evaluate its performance. Results show that a suitable location of the deputy should provide enough time to calibrate the detectors of the instrument, and that this available time is enough to perform a successful calibration, i.e., reaching a high enough number of detectors and doing so with different relative polarization orientations. This translates into having large values in all the parameters except $G(\xi)$, for which the ideal value is 0.

For the baseline scan strategy studied, the results indicate that the region near the precession axis presents the most advantageous characteristics. This is more noticeable in the case of T_{total}, ρ, and $G(\xi)$ as they experience significant variations along φ. Although T_{mean} and T_{max} remain in a narrower range of values, they also present higher values in this region.

While all the parameters present adequate values near the precession axis, there is not an optimal point where the best value of each parameter is achieved simultaneously. Moreover, a trade-off analysis should be performed according to the characteristics of the calibration process, which will indicate which parameter is more valuable.

The effect of the variation of α and β in the region is mainly the displacement of the parameters curves, with slight variations along φ. This is caused by the trace geometry. The high concentration of the trace lines when it reaches its minimum distance with the precision axis causes the peak values in the parameters. Such lines get as close as $|\alpha - \beta|$ and as this value grows, the region of maximum values is displaced to higher φ.

In comparison, other parameters have a much significant impact. The most important factor for T_{mean} and T_{max} is the value of T_{spin} as they grow proportionally to it. Although not calculated here, the time that a detector receives the signal will also be proportional to T_{spin}. Conversely, it is the T_{comb} of the two motions which mainly drives $G(\xi)$ and ρ. A high value will ensure an elevated percentage of viewed detectors and a region of low $G(\xi)$. It is clear that the higher that T_{sim} is, i.e., the longer the calibration process lasts, better values of T_{total}, $G(\xi)$ and ρ will be achieved, while T_{mean} and T_{max} will not be affected.

Although $G(\xi)$ and ρ results depend on the detectors layout, they will be similar for other layouts as long as the number of detectors is roughly the same and they cover the FoV with axial-symmetry. This condition will keep the effective area of the FoV similar and centered, which will produce analogous results as the trace of the deputy over the FoV is independent of the detectors layout.

6 Conclusions

In the present work, the visibility between a chief-deputy formation for a telescope of a scientific mission and its calibration satellite, has been studied. A typical spin and precession scan strategy has been assumed for the chief telescope. For the deputy, its visibility and access availability depends on its relative position, the chief's scanning strategy parameters and the FoV of the instrument to be calibrated.

In order to study the visibility and obtain a tool to evaluate and locate the best position for the deputy, three different time parameters have been analyzed: total access time, mean access time, and maximum access time. For each of these parameters and depending on the scanning strategy, an analytical calculation method has been presented. These analytical solutions have been validated against the results from numerical simulations of the problem, obtaining satisfactory results. The advantage of the analytical formulation is that it allows for the evaluation of the performance of different scanning strategies quickly and easily compared to the numerical approach. It also allows for sensitivity analysis to be carried out by providing a clear view of the effect that the scan strategy and relative position have in the parameter variation.

In Sect. 4, a second level of analysis has been carried out to test other characteristics of the calibration that do not have to do with access time: the percentage of calibrated instrument detectors and the variety of relative polarization orientations with which they observe the calibration source. This analysis was not well suited for analytical methods, but a numerical approach based on an instrument sensor distribution model has been proposed instead. Such a model allows us to evaluate the performance of a given calibration process at detector level and could be easily adapted to obtain other quantities and their distribution over the detectors array.

Finally, a case study based on different scanning strategy options for future scientific missions has been studied in order to test the proposed tools. Results show that the region around the precession axis presents the most favorable properties for all the parameters. Nevertheless, the final decision will be subject to a trade-off analysis according to the requirements of the particular calibration process. The results of this study provide tools to do it both rapidly and systematically.

It should be noted that, although the tools presented in this work have been used for the analysis of a satellite formation, they can be easily adapted to evaluate more generally the characteristics of the observation of each point in the sky for a given scan strategy and instrument FoV.

Acknowledgements This research was funded by the Spanish Agencia Estatal de Investigación (AEI, MICIU) by means of the project with reference PID2019-110610RB-C21.

Funding Open Access funding provided thanks to the CRUE-CSIC agreement with Springer Nature.

Declarations

Conflict of interest On behalf of all authors, the corresponding author states that there is no conflict of interest.

References

1. Ade, P.A., Aikin, R., Barkats, D., Benton, S., Bischoff, C.A., Bock, J., Bradford, K., Brevik, J., Buder, I., Bullock, E., et al.: BICEP2/Keck Array. IV. optical characterization and performance of the bicep2 and keck array experiments. Astrophys. J. **806**(2), 206 (2015)
2. Bermejo-Ballesteros, J.: Nutpy. https://gitlab.com/nutpy (2022)
3. Bermejo-Ballesteros, J., García-González, S., Cubas, J., Reinares, F.J.C., Martínez-González, E.: Development of a calibration satellite for a CMB telescope flying in formation about L2 libration point. In: EUCASS 2019, EUCASS2019-697 (2019)
4. Bock, J., Cooray, A., Hanany, S., Keating, B., Lee, A., Matsumura, T., Milligan, M., Ponthieu, N., Renbarger, T., Tran, H.: The Experimental Probe of Inflationary Cosmology (EPIC): a mission concept study for NASA's Einstein inflation probe. arXiv preprint arXiv:0805.4207 (2008)
5. Casas, F.J., Martínez-González, E., Bermejo-Ballesteros, J., García, S., Cubas, J., Vielva, P., Barreiro, R.B., Sanz, A.: L2-CalSat: A calibration satellite for ultra-sensitive CMB polarization space missions. Sensors **21**(10), 3361 (2021)
6. Delabrouille, J., Abitbol, M.H., Aghanim, N., Ali-Haïmoud, Y., Alonso, D., Alvarez, M., Banday, A.J., Bartlett, J.G., Baselmans, J., Basu, K., et al.: Microwave spectro-polarimetry of matter and radiation across space and time. arXiv preprint arXiv:1909.01591 (2019)
7. Delabrouille, J., De Bernardis, P., Bouchet, F., Achúcarro, A., Ade, P., Allison, R., Arroja, F., Artal, E., Ashdown, M., Baccigalupi, C., et al.: Exploring cosmic origins with CORE: Survey requirements and mission design. J. Cosmol. Astropart. Phys. **2018**(04), 014 (2018)
8. Diebel, J.: Representing attitude: Euler angles, unit quaternions, and rotation vectors. Matrix **58**(15–16), 1–35 (2006)
9. Dupac, X., Tauber, J.: Scanning strategy for mapping the Cosmic Microwave Background anisotropies with Planck. Astron. Astrophys. **430**(1), 363–371 (2005)
10. Gorski, K.M., Hivon, E., Banday, A.J., Wandelt, B.D., Hansen, F.K., Reinecke, M., Bartelmann, M.: Healpix: A framework for high-resolution discretization and fast analysis of data distributed on the sphere. Astrophys. J. **622**(2), 759 (2005)
11. Hanany, S., Alvarez, M., Artis, E., Ashton, P., Aumont, J., Aurlien, R., Banerji, R., Barreiro, R.B., Bartlett, J.G., Basak, S., et al.: PICO: probe of inflation and cosmic origins. arXiv preprint arXiv:1902.10541 (2019)
12. Hazumi, M., Ade, P.A., Adler, A., Allys, E., Alonso, D., Arnold, K., Auguste, D., Aumont, J., Aurlien, R., Austermann, J., et al.: LiteBIRD satellite: JAXA's new strategic L-class mission for all-sky surveys of cosmic microwave background polarization. In: Space Telescopes and Instrumentation 2020: Optical, Infrared, and Millimeter Wave, vol. 11443, p. 114432F. Int. Soc. Opt. Photonics (2020)
13. Johnson, B.R., Vourch, C.J., Drysdale, T.D., Kalman, A., Fujikawa, S., Keating, B., Kaufman, J.: A CubeSat for calibrating ground-based and sub-orbital millimeter-wave polarimeters (CalSat). J. Astron. Instrum. **4**(03n04), 1550007 (2015)
14. Price-Whelan, A.M., Sipőcz, B., Günther, H., Lim, P., Crawford, S., Conseil, S., Shupe, D., Craig, M., Dencheva, N., Ginsburg, A., et al.: The Astropy project: Building an open-science project and status of the v2.0 core package. Astron. J. **156**(3), 123 (2018)
15. Snyder, J.P., Voxland, P.M.: An album of map projections. U.S. Geological Survey professional paper, 1453. US Government Printing Office (1989)

16. Sutin, B.M., Alvarez, M., Battaglia, N., Bock, J., Bonato, M., Borrill, J., Chuss, D.T., Cooperrider, J., Crill, B., Delabrouille, J., et al.: PICO - the probe of inflation and cosmic origins. In: Space Telescopes and Instrumentation 2018: Optical, Infrared, and Millimeter Wave, vol. 10698, p. 106984F. Int. Soc. Opt. Photonics (2018)
17. Tauber, J., Nielsen, P., Martín-Polegre, A., Crill, B., Cuttaia, F., Ganga, K., Gudmundsson, J., Jones, W., Lawrence, C., Meinhold, P., et al.: Characterization of the in-flight properties of the Planck telescope. Astron. Astrophys. **622**, A55 (2019)
18. Thuong Hoang, D., Patanchon, G., Bucher, M., Matsumura, T., Banerji, R., Ishino, H., Hazumi, M., Delabrouille, J.: Bandpass mismatch error for satellite CMB experiments I: estimating the spurious signal. J. Cosmol. Astropart. Phys. **2017**(12), 015 (2017)
19. Virtanen, P., Gommers, R., Oliphant, T.E., Haberland, M., Reddy, T., Cournapeau, D., Burovski, E., Peterson, P., Weckesser, W., Bright, J., et al.: SciPy 1.0: fundamental algorithms for scientific computing in Python. Nat. Methods **17**(3), 261–272 (2020)
20. Wallis, C.G., Brown, M.L., Battye, R.A., Delabrouille, J.: Optimal scan strategies for future CMB satellite experiments. Mon. Not. R. Astron. Soc. **466**(1), 425–442 (2017)